



Groundwater level prediction in Apulia region (Southern Italy) using NARX neural network



Fabio Di Nunno^{a,b,*}, Francesco Granata^b

^a CNR-INM, Via di Vallerano, 139, 00128, Roma, Italy

^b University of Cassino and Southern Lazio, Department of Civil and Mechanical Engineering (DICEM), Via Di Biasio, 43, 03043, Cassino, Frosinone, Italy

ARTICLE INFO

Keywords:

Groundwater level prediction
Artificial neural network
NARX
Mediterranean area
Karst aquifers

ABSTRACT

In the Mediterranean area, the high water demand frequently leads to an excessive exploitation of the water resource, which involves a qualitative degradation of the freshwaters stored in coastal karst aquifers, as a result of phenomena such as sea saltwater intrusion. In this study, the NARX network was used to predict the daily groundwater level fluctuation for 76 monitored wells located on the Apulian territory. A preliminary analysis on reference wells was performed in order to assess the impact on the groundwater level prediction of two input parameters, rainfall and evapotranspiration, and the sensitivity to changes of training algorithm and input time delay. Based on the findings of the preliminary analysis, a comprehensive regional analysis and extensive sub-regional analyses were performed, proving the reliability of the NARX-BR network for the groundwater level prediction in wells located on different hydrogeological structures. The accurate results obtained for the Apulia region suggest the NARX network application for groundwater level prediction in other areas affected by groundwater resource management issues.

1. Introduction

Currently, the drinking water supply for 75% of the European population is provided by groundwater (Tulipano et al., 2005). Moreover, the issue of water availability cannot be addressed regardless of quality aspects. In the Mediterranean area, saltwater intrusion involves qualitative degradation of the freshwater resources stored in coastal karst aquifers (Polemio, 2005; Polemio et al., 2009; De Filippis et al., 2016). One of the most interesting cases is represented by Apulia (Italy). This region is characterized by average annual precipitation of approximately 600 mm, lower than the average annual precipitation of Italy, equal to about 1050 mm, and distributed mostly in winter, with storm events during the summer, as is common in the Mediterranean climate (Fiorentino et al., 2013). The lowest annual rainfall values occur in the Tavoliere area (400 mm), while the highest values in the Gargano area (1100–1200 mm). Furthermore, in the karst environments, formed from the dissolution of soluble rocks such as limestone and dolomite widespread in the region (Fig. 1), water rapidly infiltrates within the epikarst through the network of cavities and conduits (Parise, 2003). This involves a shortage availability of surface waters, increasing the uncontrolled exploitation of groundwater for irrigation, which enhances the

saltwater intrusion. These phenomena have a significant impact on the local economy, in a region where the 72% of the land is for agricultural use and the 75% of the water resources for irrigation use is provided by the groundwater (De Giglio et al., 2019). Moreover, irrigation water demand represents a leading cause of the groundwater depletion (Dong et al., 2019).

Therefore, the prediction of the groundwater level (*GWL*) is essential for the accurate management of groundwater resources. Physical-based modeling requires detailed knowledge of the study area, its characteristics, and the boundary conditions, aspects that are generally not known. At the same time, conceptual modeling requires a partial knowledge of the study area, but it does not lead to detailed results able to provide a complete understanding of the problems related to the hydrogeology of a specific study area (De Filippis, 2020). In this context, in the last few decades the black-box artificial intelligence (AI) models have taken hold. One of the most commonly used is Artificial Neural Network (ANN), applied for the groundwater quality modeling (Sahoo et al., 2005; Dixon, 2009; Cho et al., 2011) and level prediction with, as input data: rainfall and temperature (Coulibaly et al., 2001; Daliakopoulos et al., 2005; Adamowski and Chan, 2011; Juan et al., 2015), rainfall and potential evapotranspiration (Shiri et al., 2013) and

* Corresponding author. CNR-INM, Via di Vallerano, 139, 00128, Roma, Italy.

E-mail address: fabio.dinunno@unicas.it (F. Di Nunno).

neighboring wells *GWL* (Chen et al., 2010, 2011).

Wu et al. (2014) and Rajaei et al. (2019) provide a comprehensive review of ANN models for groundwater quality and level prediction, respectively.

The aim of this study is the simultaneous modeling of a network consisting of 76 wells located in the entire territory of the Apulia region. Non-linear AutoRegressive with eXogenous inputs (NARX) neural networks were applied. These dynamic recurrent neural networks are particularly suitable for the prediction of time series that highlight seasonal components, without computational losses compared to conventional ANN approaches (Guzman et al., 2017, 2018; Wunsch et al., 2018; Zhang et al., 2019; Alsumaie, 2020). A preliminary analysis of four reference wells was performed, in order to assess the evapotranspiration impact on the *GWL* prediction, considering two distinct models that, respectively, took evapotranspiration into account or not. Furthermore, the sensitivity of the results to changes in the training algorithm and input time delay was evaluated. Based on the results of the preliminary analysis, a complete regional analysis was performed. In addition, detailed studies on sub-regions, identified on the basis of their hydrogeological characteristics, were carried out. Compared to most of the existing literature on the topic, the study here presented, in addition to involving a far greater number of wells than the other literature studies, was conducted with a higher temporal resolution, considering, for each well, the daily *GWL*, rainfall and temperature data instead of monthly or weekly data.

2. Materials and methods

2.1. Study area and dataset

The Apulia region is located in the southeast part of the Italian peninsula, bordering the Adriatic and Ionian seas respectively along the east and southeast coasts. The region is characterized by low mountains located in the Daunian Sub-Appennine and in the Gargano promontory, respectively in the east and north of the Foggia (FG) province, the Murgia plateau, that covers a surface of 4000 km² in the provinces of Barletta-Andria-Trani (BT) and Bari (BA), and the Tavoliere plain, the second largest plain in Italy, which extends for 3000 km² in the central and southern part of the Foggia province. Most of the region is characterized by small plains with moderate hills, located inside the provinces of Brindisi (BR), Taranto (TA) and Lecce (LE). From a geological point of view, there are mainly limestones, clays, and dolomites formations that alternate along the region, and eolian deposits along the Arco Ionico-Tarantino in the Taranto province.

Groundwater level dataset consisted of measures on 76 monitored wells covering the entire regional territory. For each well, daily groundwater level data from February 2008 to January 2012 were used in the analysis (CNR-IRSA, 2009). It should be noted that, based on the thermo-pluviometric data measured in more recent years, no significant climatic changes were observed in the region (Apulia Region, 2019a). Therefore, the models that were developed in this study can also be used

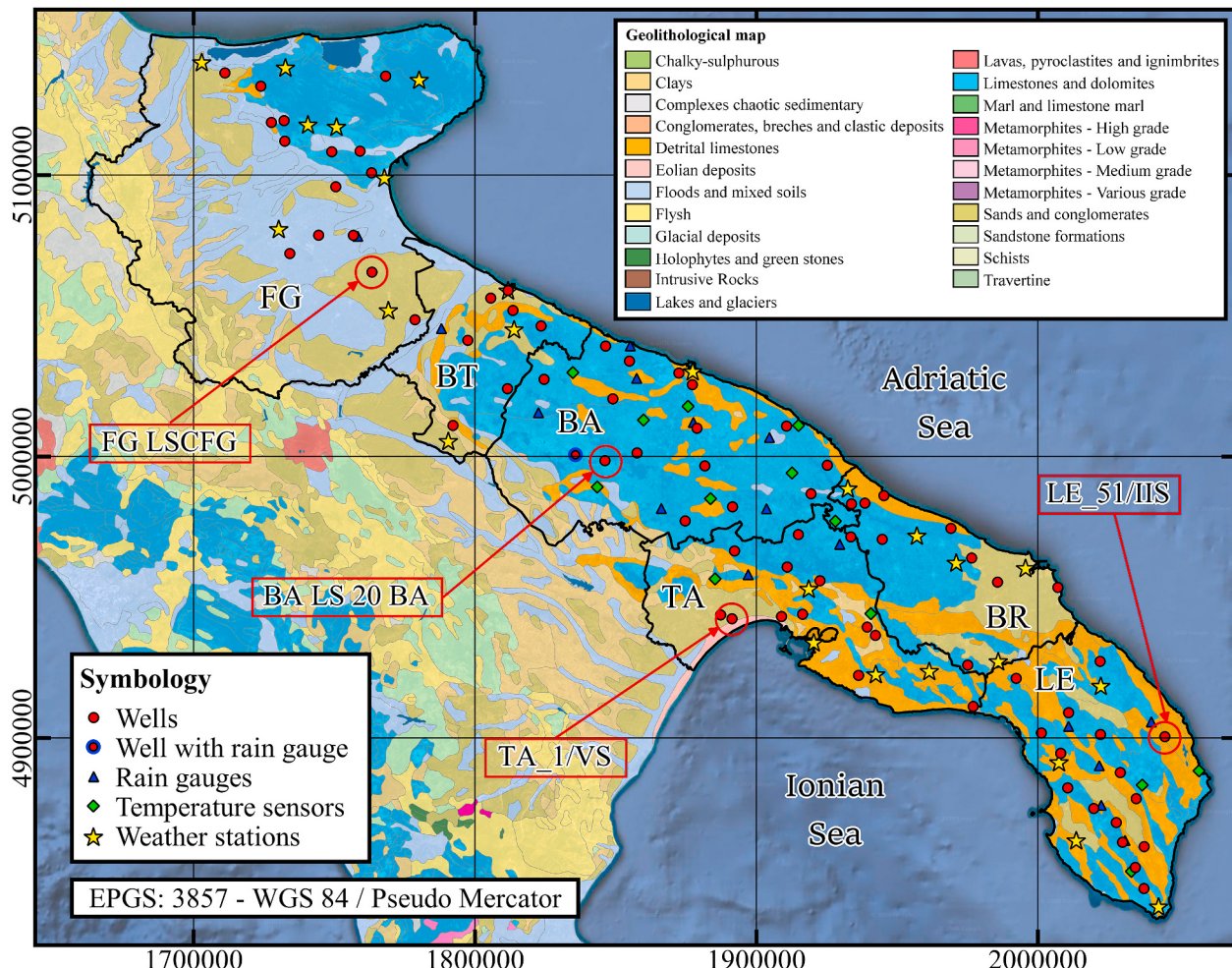


Fig. 1. Location of the wells, rain gauges and temperature sensors, with a geolithological representation of the Apulia region. Weather stations provide both daily rainfall and temperature. The four reference wells for the preliminary analysis are circled in red. (For interpretation of the references to colour in this figure legend, the reader is referred to the Web version of this article.)

in the future. Furthermore, daily rainfall P and daily maximum and minimum temperature were obtained from rain gauges and temperature sensors located at a maximum distance of 10 km from each well. Fig. 1 shows the wells, rain gauges, temperature sensors and weather stations locations in a geolithological representation of the Apulia region (ISPRA, 2011). Weather stations provide both daily rainfall and temperature.

2.2. Evapotranspiration

The groundwater level prediction was based on the daily rainfall P and potential evapotranspiration ET_p . Due to the unavailability of wind speed, humidity and solar radiation data, ET_p , expressed in mm/day, was computed with the Hargreaves-Samani (1985) equation:

$$ET_p = 0.0023 \left(\frac{T_{\max} + T_{\min}}{2} + 17.8 \right) R_a \sqrt{T_{\max} - T_{\min}} \quad (1)$$

where R_a is the extra-terrestrial solar radiation, expressed in MJ/m²·day, which depends on the days of the year and the latitude of the site. The daily maximum and minimum temperature, respectively T_{\max} and T_{\min} , are both expressed in °C. This equation provides ET_p values that are not very different from those obtained with the Penman-Monteith equation (FAO, 1998), which have a detailed theoretical base but requires the knowledge of several agro-climatological parameters (Granata, 2019; Granata et al., 2020), and adapts well to Mediterranean climates (Marini et al., 2018).

2.3. NARX model architectures

NARX networks are a particularly recurrent dynamic type of ANNs networks. ANNs are composed of a group of interconnected nodes, "artificial neurons", which retain the biological neurons. Each neuron can have multiple input-output connections, with the latter ones providing the output of one neuron as input for another one. Based on the direction of information flow and processing, it is possible to distinguish the ANNs in different categories. While in feedforward neural networks (FNNs) the nodes are arranged in layers with a one-direction flow of information, in recurrent networks, like NARX, information flows both in the forward and backward directions allowing connections between neurons in the same or previous layers (ASCE Task Committee on Application of Artificial Neural Networks in Hydrology, 2000). One of the advantages of the NARX model, in comparison with FNN, is the reduced number of input parameters to make the model more effective (Guzman et al., 2017). The equation for the NARX model is:

$$y(t) = f(y(t-1), y(t-2), \dots, y(t-n_y), u(t-1), u(t-2), \dots, u(t-n_u)) \quad (2)$$

where $u(t)$ and $y(t)$ are the input and output values at time t , n_u and n_y are the input and output network layers, and f is the non-linear function, approximating by the FNN. The NARX model was implemented with the Neural Net Time Series code in MATLAB®2020a (MathWorks, 2020). Two different NARX model architectures were used in this study. In the first, indicated as "Model I", the input values were the lagged GWL , which depends on the time delay t_d , and $u(t)$, which is the daily rainfall P , the output value $y(t)$ was the groundwater level. In the second, indicated as "Model II", the input values were the lagged GWL and $u_1(t)$ and $u_2(t)$, which are respectively the daily rainfall P and potential evapotranspiration ET_p , while the output value $y(t)$ was the groundwater level.

The time delay t_d was evaluated by means of cross-correlation function XCF between the rainfall and groundwater level time series. After calculating the cross-correlation between the time series, t_d was evaluated as the maximum point of the cross-correlation function:

$$t_{d,c} = \max(XCF) = \max \left(\int_0^s P(t)GWL(t+\tau)dt \right) \quad (3)$$

where s is the size of the time series, which is the same for P and GWL , and τ is the delay (Iannello, 1982). The predictions obtained with the computed time delay $t_{d,c}$ were compared with the ones obtained with four different values of the time delay t_d usually considered in literature and equal to 5, 25, 50 and 100 days (Guzman et al., 2017). This allowed to evaluate the performance of the models as the time delay increases. The number of hidden nodes was equal to 2, respectively h_1 and h_2 , which is indicated in literature as optimal for the GWL predictions (Coulibaly et al., 2001). For the hidden layer, a sigmoid activation function f_1 was used, while a linear activation function f_2 , with only one neuron n , was used for the output layer. The output $y(t)$ is then fed back to the input values as part of the NARX architectures. Furthermore, the weight w and bias b were optimized based on the different training algorithms described below. The architecture of the two NARX models is reported in Fig. 2.

Furthermore, a normalization of both input and output values was conducted, in order to have a common range, between 0 and 1, to improve the modeling performance. The daily rainfall and potential evapotranspiration were normalized with respect to the maximum values along the time series while the groundwater level was normalized with respect to the minimum value along the time series, which corresponds to the lower water availability:

$$P_i^* = \frac{P_i}{\max(P)} \quad (4)$$

$$ET_{p,i}^* = \frac{ET_{p,i}}{\max(ET_p)} \quad (5)$$

$$GWL_i^* = \frac{GWL_i}{\min(GWL)} \quad (6)$$

where i indicates the days.

2.4. Training algorithm

Three training algorithms were used in the present study. The first one was the Levenberg-Marquardt (*LM*), which is widely used for time series prediction by means of ANNs (Levenberg, 1944; Khaki et al., 2015; Alsumaie, 2020). It is fast and has stable convergence (Yu and Wilamowski, 2011). Basically, it is used to solve non-linear least squares problems. *LM* algorithm approximates the Hessian matrix according to the equation (Bishop, 1995):

$$\Delta w = [J^T(w)J(w) + \lambda I]^{-1} J^T(w)e(w) \quad (7)$$

where, w is the weight vector, J is the Jacobian matrix and J^T the transpose, I is the identity matrix, e is the error vector and λ is the learning constant, adjusted iteratively to find the minimum error.

The second training algorithm was the Bayesian Regularization (*BR*) which consists of a Gauss-Newton approximation to the Hessian matrix $J^T(w)J(w)$, based on the Bayesian technique proposed by MacKay (1992), implemented in the *LM* algorithm, in order to reduce the probability of overfitting and the computational overhead (Foresee, 1997).

Generally, the *LM* algorithm is faster while the *BR* algorithm works better on complex problems. A middle ground between fast convergence and accuracy is commonly represented by a third training algorithm, the Scaled Conjugate Gradient (*SCG*) (Møller, 1993; Sharma and Venugopalan, 2014; Chitsazan et al., 2015), which is an iteration algorithm used to solve problem of large systems of linear equation, according to the relation (adapted from Du and Stephanus, 2018):

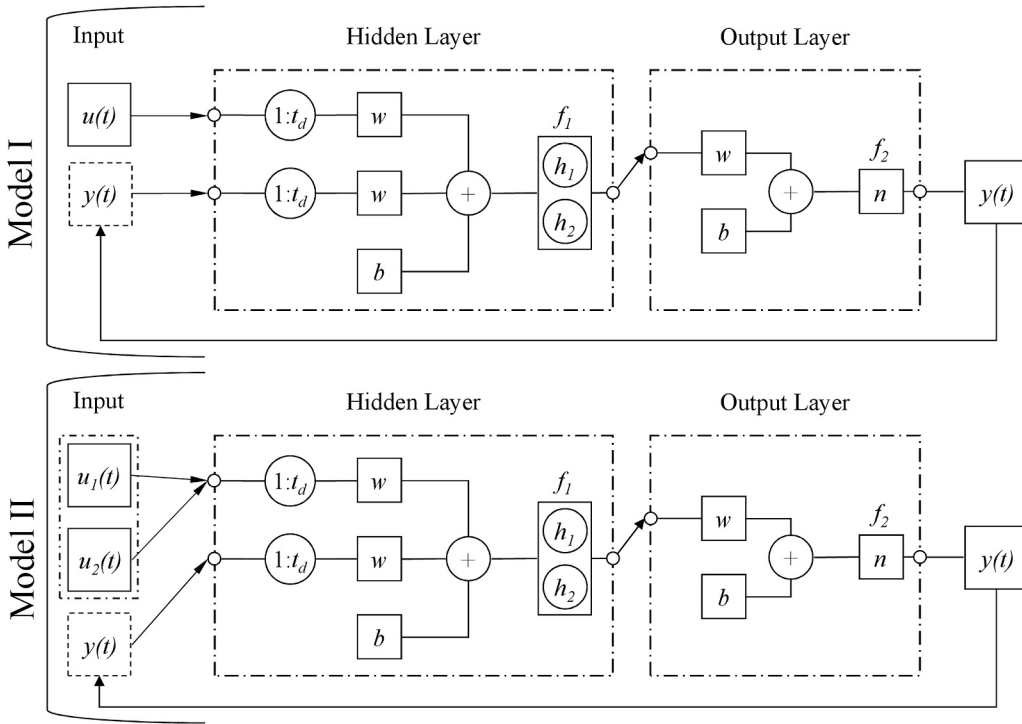


Fig. 2. Schematic of the NARX model architectures.

$$\Delta w = w_k - w_{k-1} = \alpha_k d_{k-1} \quad (8)$$

where k is the iteration index, α_k is the step length at k iteration and d_{k-1} is the search direction.

2.5. Evaluation metrics

Different evaluation metrics were used to evaluate the performance of the NARX network trained with *LM*, *BR* and *SCG* algorithms: the coefficient of determination R^2 , which allows to assess the best linear fit between measured and predicted data, the Mean Absolute Error (*MAE*), which provides the average error magnitude for the predicted values, the Root Mean Squared Error (*RMSE*), which provides the square root of the average squared errors for the predicted values, and the Relative Absolute Error (*RAE*), which is the ratio between the absolute error and the absolute value of the difference between average and each measured values. These metrics are defined as:

$$R^2 = 1 - \frac{\sum_{i=1}^m (f_i - y_i)^2}{\sum_{i=1}^m (y_a - y_i)^2} \quad (9)$$

$$MAE = \frac{\sum_{i=1}^m |f_i - y_i|}{m} \quad (10)$$

$$RMSE = \sqrt{\frac{\sum_{i=1}^m (f_i - y_i)^2}{m}} \quad (11)$$

$$RAE = \frac{\sum_{i=1}^m |f_i - y_i|}{\sum_{i=1}^m |y_a - y_i|} \quad (12)$$

where m is the total number of measured data, f_i is the predicted value for the i -th data, y_i is the experimental value for the i -th data and y_a is the averaged value of the measured data.

3. Results and discussion

3.1. Preliminary analysis on reference wells

In this section, a preliminary analysis of the *GWL* prediction on 4 of the 76 wells is reported, in order to assess the impact of evapotranspiration, training algorithms and input time delays on the prediction model performances. A comprehensive regional analysis was conducted based on the results of the preliminary analysis. In addition, a more in-depth study, linked to hydrogeological aspects, was carried out on the sub-regions in which the four reference wells are located. The latter, whose time series are reported in Figs. 3 and 4, were chosen in order to represent the different hydrogeological and morphological features of the Apulia region.

Time series were divided into three sets: the first two sets, corresponding to the period February 2, 2008–December 31, 2011, were used for the training (70% of the data) and testing (30% of the data) of the network, allowing an internal cross-validation on a portion of the dataset (Lee and Sheridan, 2018). The last year data were used as additional values for a further validation of the algorithm. From north to south, the four wells are: “FG LSCFG”, located in the Tavoliere plain area with soils formed mainly by sands and conglomerates, “BA LS 20 BA”, located in the Murgia plateau with soils formed by limestones and dolomites, “TA_1/VS”, located in the Arco Ionico-Tarantino close to the Ionian Sea with soils formed by eolian deposits, sands and conglomerates, “LE_51/IIS”, located in the Salento sub-region, close to the Adriatic Sea with soils formed by detrital limestones (see Fig. 1 for the wells location). The nomenclature reported in “Progetto Tiziano” (CNR-IRSA, 2009) was selected in the designation of the wells used in this study.

Daily *GWL* follows a fluctuating trend, with positive peaks in the period February–May, as a result of the greater rainfall of the winter season, and negative peaks during the summer, due to lower rainfall and higher water demand (Fig. 3). A challenging task is to predict these oscillations, both in terms of frequency and extent of the *GWL* fluctuations. The latter can be expressed in terms of standard deviation and are very different from well to well, passing from 0.43 m for the shallower well “LE_51/IIS”, with an average *GWL* of −8.98 m, to 7.22 m for the

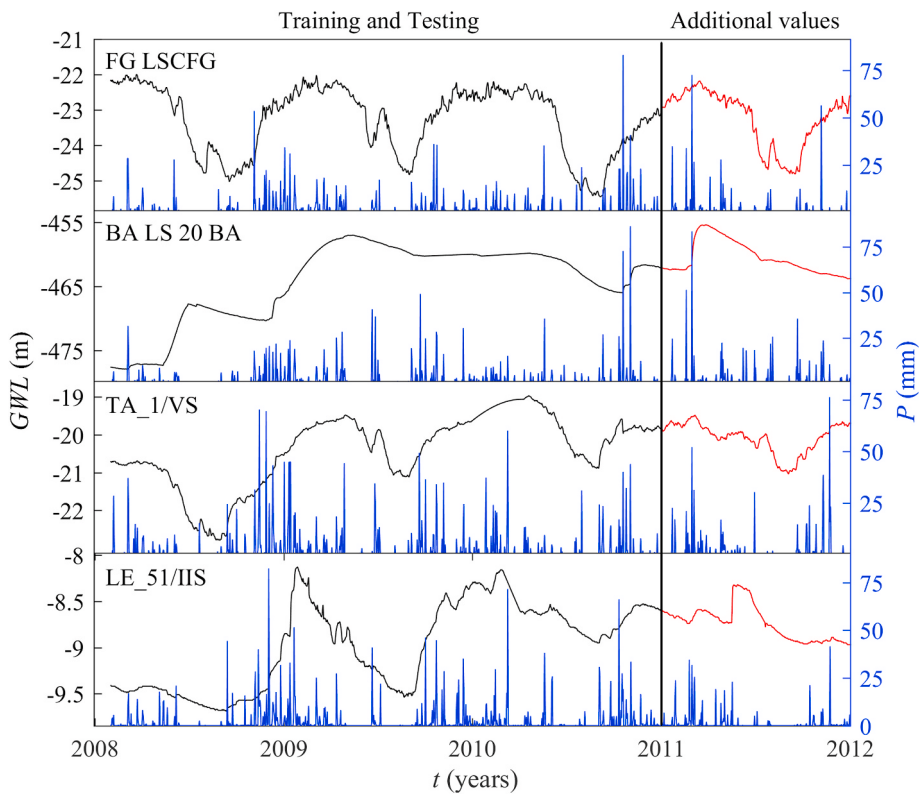


Fig. 3. Daily groundwater level and rainfall.

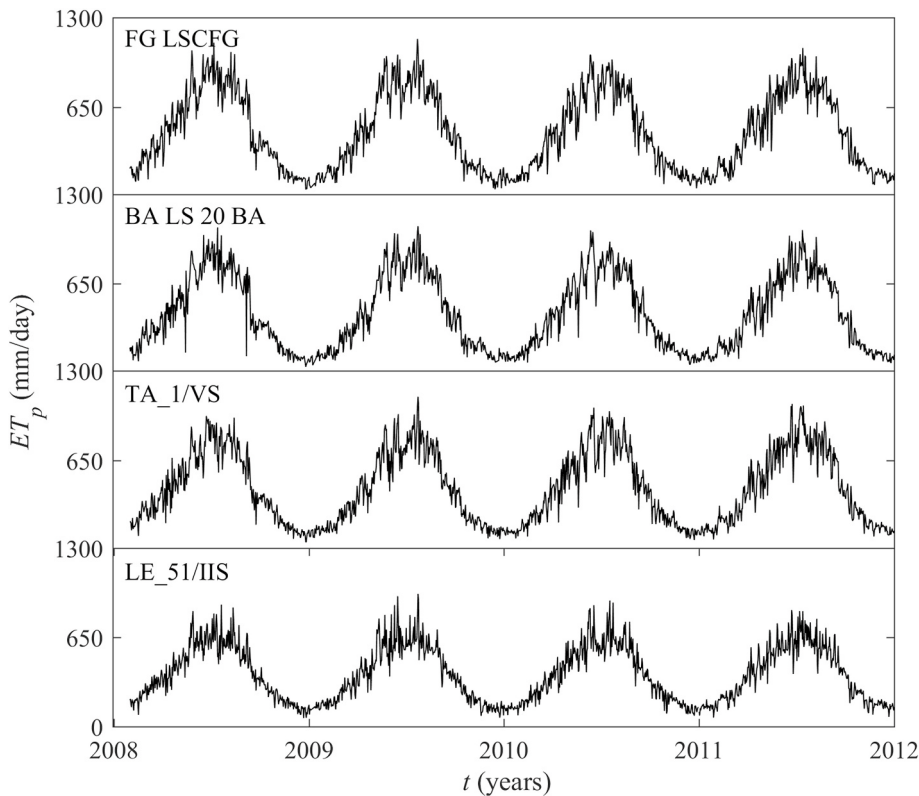


Fig. 4. Daily potential evapotranspiration.

deeper well "BA LS 20 BA", with an average GWL of -465.24 m. Overall, lower fluctuations of the piezometric levels were observed in the shallower and near-to-the-coast wells compared to the deeper ones located

in hilly areas, with some exceptions, according to the different hydrogeological structures, as explained in the following sections.

3.1.1. Time delay evaluation

Fig. 5 shows the cross-correlation function between rainfall and groundwater level for the four reference wells. Time delay was evaluated as the positive peak of the cross-correlation diagram, according to Equation (3).

The well "FG LSCFG" was characterized by the higher $t_{d,c}$, equal to 26 days. For the well "BA LS 20 BA" a slightly lower $t_{d,c}$, equal to 25 days, was evaluated. The first well is shallower ("FG LSCFG" and "BA LS 20 BA" showed respectively an average GWL of -23.26 m and -465.24 m) and closer to the sea ("FG LSCFG" and "BA LS 20 BA" are respectively at 15 km and 30 km from the Adriatic Sea). This discrepancy is justified by the different hydrogeological structures on which the wells are located. The well "BA LS 20 BA" is located in the part of the Murgia plateau characterized by karst aquifer with underground drainage systems formed from the dissolution of limestones and dolomites, leading to a rapid variation of the piezometric level following meteorological events. Instead, the well "FG LSCFG" is located on a shallow aquifer of the Tavoliere plain, with soils that consist mainly of sands and conglomerates, without being affected by phenomena related to karst environment. A similar situation to the well "FG LSCFG" was observed for "TA_1/VS" ($t_{d,c} = 21$ days) with the latter located on a multi-layered aquifer, with the shallower layer that has similar properties to the shallow aquifer in the Tavoliere area. Approaching the Salento area, the time delay values for shallow and near-to-the-coast wells were reduced by up to 4 days. For the well "LE_51/IIS", located in a karst environment, the $t_{d,c}$ was equal to 13 days, the lowest in comparison with the other three reference wells. Overall, the spatial differences of the time delay are mainly related to the different sub-regional hydrogeological properties and to a lesser extent to the GWL, in a good agreement with some literature data (Tennyson et al., 1975; Hocking and Kelly, 2016) and in apparent disagreement with other literature results. In particular, Cui et al. (2020) do not highlight an obvious difference in terms of time delay among hydrogeological zones, detecting a weaker correlation between precipitation and GWL for the confined waters compared with the unconfined ones (Cui et al., 2020). These discrepancies, frequently observed in the literature, may be related to further environmental factors as well as climatic and hydrological ones that could be the subject of future in-depth studies.

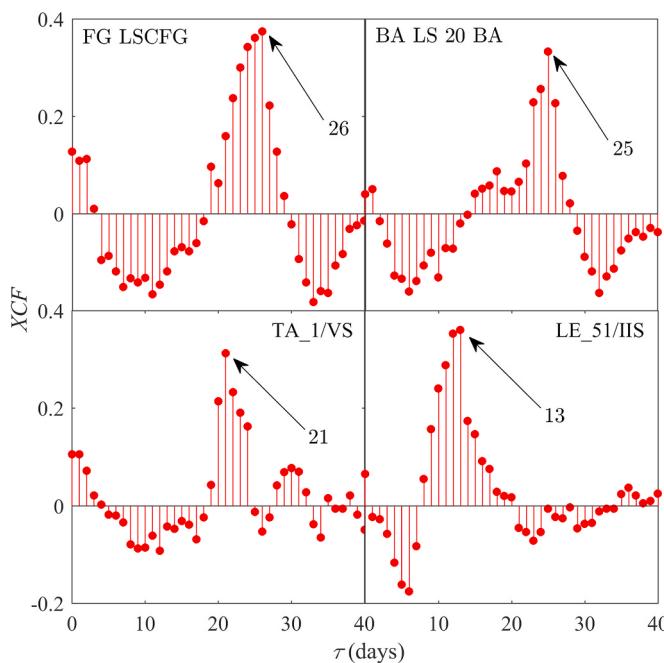


Fig. 5. Cross-correlation function for the evaluation of the time delay.

3.1.2. Training and testing

The GWL prediction for the training and testing steps are discussed in this section. The NARX-BR network provided the best forecast performance, for all the wells and time delays. NARX-LM network exhibited a similar performance but slightly lower than the NARX-BR network while NARX-SCG network gave the less accurate predictions (Table 1). For the well "BA LS 20 BA" the RMSE ranges was $5.39 \times 10^{-8} - 1.82 \times 10^{-6}$ for the Model I and $1.49 \times 10^{-7} - 2.56 \times 10^{-6}$ for the Model II while the RAE ranges was $4.14 \times 10^{-3} - 5.62 \times 10^{-3}$ for the Model I and $4.28 \times 10^{-3} - 6.02 \times 10^{-3}$ for the Model II. The performance achieved with the NARX-BR was still very accurate even for the other three reference wells. The worst performance for NARX-BR was observed for the well "FG LSCFG" and $t_d = 25$ days, with: Model I - RMSE = 1.12×10^{-4} , RAE = 5.07×10^{-2} and Model II - RMSE = 3.13×10^{-5} , RAE = 4.83×10^{-2} , which still was extremely accurate. Furthermore, despite the lower performance of the SCG training algorithms in comparison with those obtained with the LM and BR training algorithms, very good predictions were achieved also with the NARX-SCG network, e.g. for the well "TA_1/VS" and a time delay equal to the computed one ($t_{d,c} = 21$ days): Model I - RMSE = 6.97×10^{-5} , RAE = 4.72×10^{-2} , Model II - RMSE = 8.43×10^{-5} , RAE = 6.15×10^{-2} .

Fig. 6 shows the GWL prediction for the well "BA LS 20 BA" with the Model I and the four time delays. As expected based on the evaluation metrics, the difference between measured and predicted GWL* were very low (within $\pm 1.5 \times 10^{-3}$) with the NARX-BR network which is perfectly capable of capturing the positive and negative seasonal peaks.

Overall, predictions were not significantly affected by evapotranspiration as input parameter, with Models I and II that showed very similar evaluation metrics. Furthermore, the best GWL predictions were achieved with the NARX-BR network referring to the computed time delay $t_{d,c}$.

3.1.3. Validation

A further validation step of the prediction models is here reported and discussed. As for the training and testing stages, the NARX-BR network highlighted the best performance for all wells and time delays, in particular for the lowest time delay, equal to 5 days, with a slight performance decrease as the time delay increases. However, the performances were still very good for the computed time delays, e.g. for the well "TA_1/VS" and $t_{d,c} = 13$ days: Model I - RMSE = 6.69×10^{-5} , RAE = 6.58×10^{-2} , Model II - RMSE = 6.69×10^{-5} , RAE = 6.58×10^{-2} . Overall, the predictions were also very accurate for the NARX-LM network. The NARX-SCG showed the less accurate prediction with a more marked performance decay as the time delay increases, in comparison with the other two training algorithm, e.g. for "LE_51/IIS" – Model I, the ranges of the evaluation metrics, passing from $t_d = 5-100$ days, were: RMSE = $5.30 \times 10^{-4} - 2.78 \times 10^{-3}$, RAE = $7.35 \times 10^{-2} - 2.58 \times 10^{-1}$ (Table 2).

From a performance point of view, there were no substantial differences between Model I and Model II. Overall, the GWL predictions were very accurate regardless of whether or not evapotranspiration is considered as an input parameter for the NARX network. This confirms the greater forecasting potential of the NARX networks compared to other ANNs, which required more input parameters for an accurate GWL prediction, e.g. radial basis function network (Coulibaly et al., 2001; Daliakopoulos et al., 2005) or multilayer perceptron (Adamowski and Chan, 2011), which require rainfall and temperature as input parameters for the GWL forecasting.

A further comparison between the results obtained with the three different training algorithms with only rainfall as input value (Model I) is shown in Fig. 7, that reports a notched box plots representation of the GWL prediction, representing the relative errors, equal to the ratio between the measured-predicted difference and the measured values, for the well "BA LS 20 BA". A negative GWL change corresponds to a rise of the water level (Equation (6)). Therefore, a negative relative error involves an overestimation of the water rise or led to an underestimation

Table 1

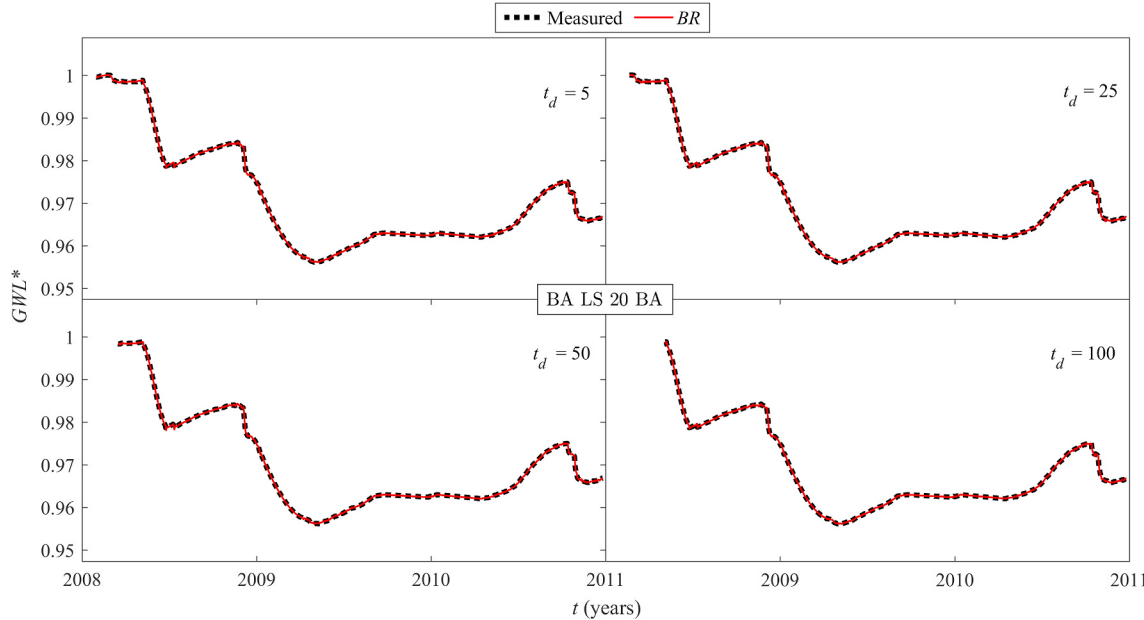
Prediction performance in the training and testing of the NARX network for the different time delays (including computed time delays $t_{d,c}$, indicated with asterisks) and training algorithms, for both Models I and II. **NARX-BR**, indicated in bold, provides the best prediction performance.

Wells	t_d (days)	NARX-LM				NARX-BR				NARX-SCG			
		R ²	MAE	RMSE	RAE	R ²	MAE	RMSE	RAE	R ²	MAE	RMSE	RAE
Model I													
FG LSCFG	5	0.99621	1.70 × 10^{-3}	1.26 × 10^{-5}	5.21 × 10^{-2}	0.99627	1.68 × 10^{-3}	1.12 × 10^{-6}	5.14 × 10^{-2}	0.99508	1.96 × 10^{-3}	4.33 × 10^{-5}	5.98 × 10^{-2}
	25	0.99628	1.68 × 10^{-3}	1.33 × 10^{-6}	5.13 × 10^{-2}	0.99637	1.66 × 10^{-3}	1.12 × 10^{-4}	5.07 × 10^{-2}	0.97857	4.16 × 10^{-3}	2.89 × 10^{-5}	1.27 × 10^{-1}
	26*	0.99627	1.66 × 10^{-3}	7.10 × 10^{-5}	5.07 × 10^{-2}	0.99638	1.66 × 10^{-3}	7.02 × 10^{-5}	5.06 × 10^{-5}	0.98096	3.97 × 10^{-3}	1.60 × 10^{-4}	1.21 × 10^{-1}
	50	0.99610	1.73 × 10^{-3}	2.20 × 10^{-5}	5.32 × 10^{-2}	0.99657	1.63 × 10^{-3}	2.67 × 10^{-5}	5.01 × 10^{-2}	0.98959	2.89 × 10^{-3}	7.77 × 10^{-5}	8.88 × 10^{-2}
	100	0.99546	1.89 × 10^{-3}	2.92 × 10^{-4}	5.85 × 10^{-2}	0.99663	1.57 × 10^{-3}	1.47 × 10^{-5}	4.85 × 10^{-2}	0.98592	3.30 × 10^{-3}	1.56 × 10^{-4}	1.02 × 10^{-1}
BA LS 20	5	0.99996	4.30 × 10^{-5}	8.01 × 10^{-7}	4.09 × 10^{-3}	0.99995	4.35 × 10^{-5}	2.00 × 10^{-7}	4.14 × 10^{-3}	0.97840	1.29 × 10^{-3}	1.40 × 10^{-5}	1.23 × 10^{-1}
	25*	0.99994	5.66 × 10^{-5}	5.76 × 10^{-9}	5.63 × 10^{-3}	0.99996	4.30 × 10^{-5}	5.39 × 10^{-8}	4.28 × 10^{-3}	0.98933	9.42 × 10^{-4}	2.92 × 10^{-5}	9.38 × 10^{-2}
	50	0.99994	5.20 × 10^{-5}	4.21 × 10^{-7}	5.52 × 10^{-3}	0.99994	4.78 × 10^{-5}	1.82 × 10^{-6}	5.07 × 10^{-3}	0.98568	1.04 × 10^{-3}	6.11 × 10^{-6}	1.11 × 10^{-1}
	100	0.99992	5.37 × 10^{-5}	2.38 × 10^{-5}	6.67 × 10^{-3}	0.99994	4.52 × 10^{-5}	3.25 × 10^{-8}	5.62 × 10^{-3}	0.98878	7.32 × 10^{-4}	1.28 × 10^{-5}	9.09 × 10^{-2}
TA_1/VS	5	0.99927	7.44 × 10^{-4}	3.47 × 10^{-5}	2.20 × 10^{-2}	0.99929	7.25 × 10^{-4}	1.23 × 10^{-5}	2.14 × 10^{-2}	0.97786	4.57 × 10^{-3}	8.34 × 10^{-4}	1.35 × 10^{-1}
	21*	0.99934	7.40 × 10^{-4}	3.31 × 10^{-5}	2.17 × 10^{-2}	0.99939	7.06 × 10^{-4}	3.18 × 10^{-5}	2.07 × 10^{-2}	0.99707	1.61 × 10^{-3}	6.97 × 10^{-5}	4.72 × 10^{-2}
	25	0.99937	7.23 × 10^{-4}	5.48 × 10^{-6}	2.12 × 10^{-2}	0.99935	7.37 × 10^{-4}	2.17 × 10^{-5}	2.16 × 10^{-2}	0.98867	3.19 × 10^{-3}	2.91 × 10^{-4}	9.36 × 10^{-2}
	50	0.99931	7.85 × 10^{-4}	3.89 × 10^{-5}	2.28 × 10^{-2}	0.99939	7.39 × 10^{-4}	8.60 × 10^{-6}	2.14 × 10^{-2}	0.99381	2.58 × 10^{-3}	8.88 × 10^{-5}	7.47 × 10^{-2}
	100	0.99903	9.69 × 10^{-4}	1.06 × 10^{-5}	2.76 × 10^{-2}	0.99941	7.21 × 10^{-4}	2.54 × 10^{-5}	2.05 × 10^{-2}	0.97066	5.78 × 10^{-3}	3.05 × 10^{-4}	1.64 × 10^{-1}
LE_51/IIS	5	0.99851	1.11 × 10^{-3}	1.41 × 10^{-4}	2.59 × 10^{-2}	0.99872	9.29 × 10^{-4}	2.02 × 10^{-5}	2.16 × 10^{-2}	0.99831	1.18 × 10^{-3}	3.53 × 10^{-5}	2.74 × 10^{-2}
	13*	0.99865	9.66 × 10^{-4}	5.39 × 10^{-5}	2.25 × 10^{-2}	0.99874	9.76 × 10^{-4}	5.21 × 10^{-5}	2.28 × 10^{-2}	0.99716	1.73 × 10^{-3}	7.82 × 10^{-5}	4.03 × 10^{-2}
	25	0.99870	1.05 × 10^{-3}	6.88 × 10^{-6}	2.46 × 10^{-2}	0.99873	9.45 × 10^{-4}	2.83 × 10^{-5}	2.21 × 10^{-2}	0.98489	4.46 × 10^{-3}	2.60 × 10^{-5}	1.04 × 10^{-1}
	50	0.99846	1.29 × 10^{-3}	6.34 × 10^{-5}	3.04 × 10^{-2}	0.99888	9.49 × 10^{-4}	5.95 × 10^{-5}	2.25 × 10^{-2}	0.98368	4.61 × 10^{-3}	4.79 × 10^{-5}	1.09 × 10^{-1}
	100	0.99866	1.08 × 10^{-3}	9.95 × 10^{-5}	2.61 × 10^{-2}	0.99893	9.09 × 10^{-4}	1.27 × 10^{-5}	2.20 × 10^{-2}	0.98607	4.17 × 10^{-3}	5.71 × 10^{-6}	1.01 × 10^{-1}
Model II													
FG LSCFG	5	0.99616	1.70 × 10^{-3}	1.44 × 10^{-5}	5.19 × 10^{-2}	0.99645	1.63 × 10^{-3}	4.15 × 10^{-5}	4.99 × 10^{-2}	0.99526	1.90 × 10^{-3}	1.59 × 10^{-4}	5.76 × 10^{-2}
	25*	0.99647	1.66 × 10^{-3}	1.06 × 10^{-4}	5.07 × 10^{-2}	0.99671	1.58 × 10^{-3}	3.13 × 10^{-5}	4.83 × 10^{-2}	0.98685	3.33 × 10^{-3}	1.84 × 10^{-4}	9.83 × 10^{-2}
	26*	0.99629	1.68 × 10^{-3}	7.08 × 10^{-5}	5.13 × 10^{-2}	0.99641	1.65 × 10^{-3}	6.97 × 10^{-5}	5.06 × 10^{-2}	0.96639	5.22 × 10^{-3}	2.13 × 10^{-4}	1.60 × 10^{-1}
	50	0.99648	1.64 × 10^{-3}	9.01 × 10^{-5}	5.05 × 10^{-2}	0.99704	1.51 × 10^{-3}	6.62 × 10^{-6}	4.64 × 10^{-2}	0.98629	3.32 × 10^{-3}	1.92 × 10^{-4}	1.02 × 10^{-1}
	100	0.99110	2.63 × 10^{-3}	1.66 × 10^{-4}	8.11 × 10^{-2}	0.99703	1.47 × 10^{-3}	5.46 × 10^{-5}	4.55 × 10^{-2}	0.98297	3.88 × 10^{-3}	2.19 × 10^{-4}	1.14 × 10^{-1}
BA LS 20	5	0.99993	6.94 × 10^{-5}	1.60 × 10^{-6}	6.61 × 10^{-3}	0.99993	6.33 × 10^{-5}	1.49 × 10^{-7}	6.02 × 10^{-3}	0.99782	4.11 × 10^{-4}	3.51 × 10^{-5}	3.91 × 10^{-2}
	25*	0.99995	5.03 × 10^{-5}	2.82 × 10^{-6}	5.00 × 10^{-3}	0.99997	4.30 × 10^{-5}	2.34 × 10^{-7}	4.28 × 10^{-3}	0.99663	5.42 × 10^{-4}	1.08 × 10^{-5}	5.39 × 10^{-2}
	50	0.99994	5.42 × 10^{-5}	1.02 × 10^{-6}	5.75 × 10^{-3}	0.99995	4.58 × 10^{-5}	1.08 × 10^{-6}	4.85 × 10^{-3}	0.99548	5.96 × 10^{-4}	4.00 × 10^{-6}	6.33 × 10^{-2}
	100	0.99993	4.67 × 10^{-5}	1.16 × 10^{-6}	5.80 × 10^{-3}	0.99994	5.00 × 10^{-5}	2.56 × 10^{-6}	6.21 × 10^{-3}	0.99034	7.49 × 10^{-4}	5.11 × 10^{-5}	8.77 × 10^{-2}
TA_1/VS	5	0.99935	7.18 × 10^{-4}	4.03 × 10^{-5}	2.12 × 10^{-2}	0.99933	7.07 × 10^{-4}	1.62 × 10^{-5}	2.09 × 10^{-2}	0.99172	2.74 × 10^{-3}	1.35 × 10^{-4}	8.11 × 10^{-2}
	21*	0.99935	7.36 × 10^{-4}	3.29 × 10^{-5}	2.16 × 10^{-2}	0.99937	7.30 × 10^{-4}	3.25 × 10^{-5}	2.14 × 10^{-2}	0.99572	2.10 × 10^{-3}	8.43 × 10^{-5}	6.15 × 10^{-2}
	25	0.99939	7.06 × 10^{-4}	5.81 × 10^{-6}	2.07 × 10^{-2}	0.99937	7.42 × 10^{-4}	2.32 × 10^{-5}	2.17 × 10^{-2}	0.98917	3.30 × 10^{-3}	2.44 × 10^{-4}	9.68 × 10^{-2}
	50	0.99939	7.58 × 10^{-4}	4.29 × 10^{-5}	2.20 × 10^{-2}	0.99948	6.85 × 10^{-4}	1.27 × 10^{-5}	1.99 × 10^{-2}	0.99681	1.78 × 10^{-3}	1.97 × 10^{-5}	5.16 × 10^{-2}
	100	0.99936	7.99 × 10^{-4}	1.64 × 10^{-4}	2.27 × 10^{-2}	0.99942	6.76 × 10^{-4}	2.76 × 10^{-5}	1.92 × 10^{-2}	0.99520	2.25 × 10^{-3}	5.50 × 10^{-5}	6.40 × 10^{-2}
LE_51/IIS	5	0.99871	9.52 × 10^{-4}	1.51 × 10^{-4}	2.22 × 10^{-2}	0.99874	9.70 × 10^{-4}	2.15 × 10^{-5}	2.26 × 10^{-2}	0.99767	1.57 × 10^{-3}	4.13 × 10^{-5}	3.65 × 10^{-2}
	13*	0.99869	9.26 × 10^{-4}	5.31 × 10^{-5}	2.16 × 10^{-2}	0.99881	9.74 × 10^{-4}	5.06 × 10^{-5}	2.27 × 10^{-2}	0.99556	2.15 × 10^{-3}	9.79 × 10^{-5}	5.01 × 10^{-2}

(continued on next page)

Table 1 (continued)

Wells	t_d (days)	NARX-LM				NARX-BR				NARX-SCG			
		R ²	MAE	RMSE	RAE	R ²	MAE	RMSE	RAE	R ²	MAE	RMSE	RAE
25	0.99875	1.03 × 10^{-3}	4.48 × 10^{-7}	2.41 × 10^{-2}	0.99895	1.03 × 10^{-3}	1.91 × 10^{-5}	2.40 × 10^{-2}	0.98131	4.96 × 10^{-3}	1.19 × 10^{-4}	1.16 × 10^{-1}	
50	0.99889	1.02 × 10^{-3}	4.93 × 10^{-5}	2.41 × 10^{-2}	0.99888	1.01 × 10^{-3}	3.61 × 10^{-5}	2.39 × 10^{-2}	0.99249	3.07 × 10^{-3}	3.97 × 10^{-6}	7.26 × 10^{-2}	
100	0.99870	1.11 × 10^{-3}	1.97 × 10^{-5}	2.68 × 10^{-2}	0.99901	9.57 × 10^{-4}	4.25 × 10^{-5}	2.31 × 10^{-2}	0.98712	4.15 × 10^{-3}	2.96 × 10^{-4}	1.00 × 10^{-1}	

**Fig. 6.** GWL prediction for the well "BA LS 20 BA": NARX-BR - Model I.

of the lowering of the water level, while the opposite happens for a positive relative error. The median relative errors were close to zero for both NARX-LM and NARX-BR while increases with the increase of the time delay for NARX-SCG, leading to an overestimation of groundwater lowering or underestimation of groundwater rise. For NARX-LM and NARX-BR relative errors were between -2.5×10^{-3} and 2.5×10^{-3} , with a normal distribution of the relative errors (symmetrical notch) for t_d between 5 days and 75 days, and a slightly asymmetrical distribution for $t_d = 100$ days, with a greater concentration of negative relative errors but very close to zero, between -6.4×10^{-5} and 0 for NARX-LM and between -1.1×10^{-4} and 0 for NARX-BR, proving the accurate prediction for the tested time delays. This confirm the lower capability of the NARX-SCG, in comparison to NARX-LM and NARX-BR, to make predictions for wells characterized by less regularity of the oscillations related to seasonal phenomena and predominant impact of other factors, such as hydrogeological ones.

The comparison between measured and predicted GWL confirms for the four reference wells what was stated through the notched box plots: accurate predictions and minimal related errors were observed (Fig. 8). The best performance was obtained for "BA LS 20 BA" with relative errors within $\pm 2 \times 10^{-3}$. Slightly lower but still very good performances were observed for "TA_1/VS" with relative errors within $\pm 7.5 \times 10^{-3}$ and for "FG LSCFG" and "LE_15/IIS", with relative errors within ± 0.015 .

3.2. Regional analysis

The preliminary analysis has highlighted the low influence of evapotranspiration on the GWL prediction, with accurate and similar results for Models I and II, both in the training, testing, and validation

steps, in agreements with what highlighted by De Filippis et al. (2013) for the karst aquifers of the Salento area. Furthermore, while in the training and testing step the best predictions were obtained for the computed time delay, this does not happen for the validation step, with a performance decay as the time delay increases, in agreement with literature results (Guzman et al., 2017). Moreover, the comparison between the three training algorithms clearly showed a better accuracy of the results for the NARX-BR network, which also highlighted the less marked performance decay as the time delay increases.

Based on this observations, a regional modeling was conducted on additional wells by implementing the Model I architecture with the Bayesian Regularization as training algorithm and setting the time delays equal to those computed ($t_{d,c}$).

The R^2 and RAE scattered maps for all the 76 wells are shown in Fig. 9. The best performances were observed for different wells located on karst and deep aquifers, e.g. the well "FG_A6" ($RMSE = 4.55 \times 10^{-6}$, $RAE = 1.08 \times 10^{-2}$) in the Gargano area, with an average GWL of -166.26 m and GWL fluctuation, expressed in terms of standard deviation, equal to 1.11 m, and the well "TA_LS 2 TA" ($RMSE = 6.31 \times 10^{-6}$, $RAE = 1.84 \times 10^{-2}$) in the Itria Valley, located on the border of the Bari, Brindisi and Taranto provinces, with average GWL equal to -298.99 m and GWL fluctuation equal to 2.16 m. However, very accurate GWL predictions were also observed for wells located in flat areas on shallow aquifers, e.g. the well "FG_LS B FG" ($RMSE = 9.02 \times 10^{-5}$, $RAE = 2.06 \times 10^{-2}$) in the Tavoliere area, with average GWL equal to -10.49 m and GWL fluctuation equal to 1.79 m.

A comprehensive framework of the regional GWL prediction is given in Table 3, with a statistical analysis that consists of the evaluation of the minimum, maximum, mean, and standard deviation values of the

Table 2

Prediction performance in the NARX network validation step for the different time delays (including computed time delays $t_{d,c}$, indicated with asterisks) and training algorithms, for both Models I and II. **NARX-BR**, indicated in bold, provides the best prediction performance.

Wells	t_d (days)	NARX-LM				NARX-BR				NARX-SCG			
		R ²	MAE	RMSE	RAE	R ²	MAE	RMSE	RAE	R ²	MAE	RMSE	RAE
Model I													
FG LSCFG	5	0.99479	1.64 × 10^{-3}	1.29 × 10^{-5}	5.97 × 10^{-2}	0.99448	1.69 × 10^{-3}	2.25 × 10^{-4}	6.15 × 10^{-2}	0.99375	1.83 × 10^{-3}	2.13 × 10^{-4}	6.65 × 10^{-2}
	25	0.99356	1.90 × 10^{-3}	2.76 × 10^{-5}	6.77 × 10^{-2}	0.99430	1.78 × 10^{-3}	3.83 × 10^{-4}	6.32 × 10^{-2}	0.95573	5.56 × 10^{-3}	1.90 × 10^{-3}	1.98 × 10^{-1}
	26*	0.99531	1.70 × 10^{-3}	1.27 × 10^{-4}	5.87 × 10^{-2}	0.99486	1.78 × 10^{-3}	1.33 × 10^{-4}	6.12 × 10^{-2}	0.99259	2.14 × 10^{-3}	1.59 × 10^{-4}	7.38 × 10^{-2}
	50	0.99380	1.90 × 10^{-3}	3.94 × 10^{-4}	6.65 × 10^{-2}	0.99314	2.02 × 10^{-3}	4.19 × 10^{-4}	7.10 × 10^{-2}	0.97669	4.03 × 10^{-3}	1.46 × 10^{-3}	1.42 × 10^{-1}
	100	0.98699	2.76 × 10^{-3}	1.63 × 10^{-3}	1.02 × 10^{-1}	0.98953	2.37 × 10^{-3}	1.17 × 10^{-3}	8.72 × 10^{-2}	0.97037	4.00 × 10^{-3}	1.35 × 10^{-3}	1.47 × 10^{-1}
BA LS 20 BA	5	0.99927	8.08 × 10^{-5}	1.81 × 10^{-5}	1.70 × 10^{-2}	0.99921	6.62 × 10^{-5}	1.12 × 10^{-5}	1.39 × 10^{-2}	0.96680	5.97 × 10^{-4}	4.58 × 10^{-5}	1.25 × 10^{-1}
	25*	0.99895	1.01 × 10^{-4}	9.84 × 10^{-6}	2.07 × 10^{-2}	0.99901	9.62 × 10^{-5}	9.62 × 10^{-6}	2.00 × 10^{-2}	0.97665	5.49 × 10^{-4}	4.68 × 10^{-5}	1.14 × 10^{-1}
	50	0.99703	2.18 × 10^{-4}	2.22 × 10^{-5}	4.38 × 10^{-2}	0.99876	9.50 × 10^{-5}	3.74 × 10^{-5}	1.91 × 10^{-2}	0.91003	1.12 × 10^{-3}	1.42 × 10^{-4}	2.36 × 10^{-1}
	100	0.99557	2.43 × 10^{-4}	1.07 × 10^{-4}	6.03 × 10^{-2}	0.99371	3.02 × 10^{-4}	5.24 × 10^{-5}	7.50 × 10^{-2}	0.91138	9.15 × 10^{-4}	1.91 × 10^{-4}	2.55 × 10^{-1}
TA_1/VS	5	0.99560	9.82 × 10^{-4}	3.10 × 10^{-5}	6.57 × 10^{-2}	0.99549	1.00 × 10^{-3}	2.13 × 10^{-5}	6.72 × 10^{-2}	0.99264	1.29 × 10^{-3}	1.15 × 10^{-4}	8.64 × 10^{-2}
	21*	0.99476	1.08 × 10^{-3}	7.42 × 10^{-5}	7.17 × 10^{-2}	0.99560	9.93 × 10^{-4}	6.96 × 10^{-5}	6.58 × 10^{-2}	0.98838	1.61 × 10^{-3}	1.13 × 10^{-4}	1.07 × 10^{-1}
	25	0.99430	1.14 × 10^{-3}	3.18 × 10^{-5}	7.60 × 10^{-2}	0.99499	1.04 × 10^{-3}	1.81 × 10^{-4}	6.94 × 10^{-2}	0.98096	2.11 × 10^{-3}	8.23 × 10^{-5}	1.40 × 10^{-1}
	50	0.99404	1.15 × 10^{-3}	7.90 × 10^{-5}	7.60 × 10^{-2}	0.99443	1.11 × 10^{-3}	1.92 × 10^{-4}	7.37 × 10^{-2}	0.95643	3.16 × 10^{-3}	1.78 × 10^{-4}	2.09 × 10^{-1}
	100	0.98952	1.48 × 10^{-3}	3.30 × 10^{-4}	9.94 × 10^{-2}	0.98920	1.48 × 10^{-3}	8.34 × 10^{-4}	9.96 × 10^{-2}	0.94129	3.51 × 10^{-3}	1.94 × 10^{-3}	2.34 × 10^{-1}
LE_51/IIS	5	0.99038	1.08 × 10^{-3}	6.75 × 10^{-4}	6.40 × 10^{-2}	0.99210	7.27 × 10^{-4}	1.64 × 10^{-4}	4.29 × 10^{-2}	0.98682	1.24 × 10^{-3}	5.30 × 10^{-4}	7.35 × 10^{-2}
	13*	0.99200	7.57 × 10^{-4}	9.86 × 10^{-5}	4.44 × 10^{-2}	0.99141	8.15 × 10^{-4}	1.03 × 10^{-4}	4.85 × 10^{-2}	0.96244	2.55 × 10^{-3}	2.14 × 10^{-4}	1.50 × 10^{-1}
	25	0.98645	1.27 × 10^{-3}	4.86 × 10^{-4}	7.33 × 10^{-2}	0.99061	9.33 × 10^{-4}	1.14 × 10^{-4}	5.40 × 10^{-2}	0.97970	1.86 × 10^{-3}	1.81 × 10^{-4}	1.11 × 10^{-1}
	50	0.98412	1.72 × 10^{-3}	6.34 × 10^{-4}	9.51 × 10^{-2}	0.98936	1.19 × 10^{-3}	4.15 × 10^{-6}	6.59 × 10^{-2}	0.96207	2.92 × 10^{-3}	7.77 × 10^{-4}	1.66 × 10^{-1}
	100	0.98132	2.01 × 10^{-3}	2.75 × 10^{-4}	1.07 × 10^{-1}	0.98159	1.85 × 10^{-3}	1.19 × 10^{-3}	9.87 × 10^{-2}	0.90035	4.77 × 10^{-3}	2.78 × 10^{-3}	2.58 × 10^{-1}
Model II													
FG LSCFG	5	0.99501	1.60 × 10^{-3}	2.82 × 10^{-4}	5.82 × 10^{-2}	0.99469	1.67 × 10^{-3}	4.81 × 10^{-4}	6.09 × 10^{-2}	0.98833	2.63 × 10^{-3}	2.61 × 10^{-4}	9.55 × 10^{-2}
	25	0.99303	2.05 × 10^{-3}	6.17 × 10^{-4}	7.29 × 10^{-2}	0.99333	1.95 × 10^{-3}	6.48 × 10^{-4}	6.92 × 10^{-2}	0.97537	3.85 × 10^{-3}	5.64 × 10^{-4}	1.37 × 10^{-1}
	26*	0.99369	1.87 × 10^{-3}	1.40 × 10^{-4}	6.66 × 10^{-2}	0.99425	1.79 × 10^{-3}	1.33 × 10^{-4}	6.36 × 10^{-2}	0.92534	7.26 × 10^{-3}	4.81 × 10^{-4}	2.58 × 10^{-1}
	50	0.99187	2.21 × 10^{-3}	2.06 × 10^{-4}	7.77 × 10^{-2}	0.99248	2.12 × 10^{-3}	5.56 × 10^{-4}	7.44 × 10^{-2}	0.98484	3.37 × 10^{-3}	8.75 × 10^{-4}	1.11 × 10^{-1}
	100	0.98706	3.11 × 10^{-3}	7.78 × 10^{-4}	9.52 × 10^{-2}	0.98537	2.83 × 10^{-3}	6.54 × 10^{-4}	1.04 × 10^{-1}	0.97062	4.73 × 10^{-3}	3.28 × 10^{-4}	1.45 × 10^{-1}
BA LS 20 BA	5	0.99910	8.48 × 10^{-5}	3.93 × 10^{-2}	1.78 × 10^{-2}	0.99578	2.19 × 10^{-4}	5.88 × 10^{-5}	4.61 × 10^{-2}	0.98852	4.69 × 10^{-4}	3.99 × 10^{-5}	9.87 × 10^{-2}
	25*	0.99865	1.04 × 10^{-4}	1.45 × 10^{-5}	2.15 × 10^{-2}	0.99873	1.22 × 10^{-4}	1.47 × 10^{-5}	2.52 × 10^{-2}	0.97216	1.55 × 10^{-3}	3.38 × 10^{-5}	1.53 × 10^{-1}
	50	0.99606	2.64 × 10^{-4}	1.52 × 10^{-5}	5.31 × 10^{-2}	0.99773	1.98 × 10^{-4}	3.07 × 10^{-5}	3.98 × 10^{-2}	0.92497	1.10 × 10^{-3}	4.00 × 10^{-4}	4.59 × 10^{-1}
	100	0.98947	4.01 × 10^{-4}	1.07 × 10^{-4}	9.96 × 10^{-2}	0.98037	5.20 × 10^{-4}	2.93 × 10^{-4}	1.29 × 10^{-1}	0.92914	8.65 × 10^{-4}	6.74 × 10^{-4}	2.41 × 10^{-1}
TA_1/VS	5	0.99485	1.05 × 10^{-3}	1.40 × 10^{-4}	6.99 × 10^{-2}	0.99523	1.02 × 10^{-3}	1.37 × 10^{-5}	6.84 × 10^{-2}	0.99245	1.31 × 10^{-3}	2.60 × 10^{-4}	8.75 × 10^{-2}
	21*	0.99476	1.08 × 10^{-3}	7.42 × 10^{-5}	7.17 × 10^{-2}	0.99455	1.11 × 10^{-3}	7.56 × 10^{-5}	7.36 × 10^{-2}	0.97398	2.45 × 10^{-3}	1.65 × 10^{-4}	1.63 × 10^{-1}
	25	0.99415	1.15 × 10^{-3}	1.14 × 10^{-4}	7.66 × 10^{-2}	0.99223	1.31 × 10^{-3}	7.10 × 10^{-5}	8.70 × 10^{-2}	0.94666	3.32 × 10^{-3}	1.39 × 10^{-4}	2.21 × 10^{-1}
	50	0.99418	1.11 × 10^{-3}	1.24 × 10^{-4}	7.33 × 10^{-2}	0.99026	1.46 × 10^{-3}	1.90 × 10^{-4}	9.67 × 10^{-2}	0.92615	4.10 × 10^{-3}	2.11 × 10^{-4}	2.73 × 10^{-1}
	100	0.98644	1.61 × 10^{-3}	5.67 × 10^{-5}	1.02 × 10^{-1}	0.99035	1.35 × 10^{-3}	7.64 × 10^{-4}	8.61 × 10^{-2}	0.91600	4.30 × 10^{-3}	7.31 × 10^{-4}	2.76 × 10^{-1}
LE_51/IIS	5	0.99145	8.73 × 10^{-4}	5.01 × 10^{-4}	5.15 × 10^{-2}	0.99162	7.82 × 10^{-4}	2.18 × 10^{-4}	4.62 × 10^{-2}	0.96964	2.35 × 10^{-3}	1.52 × 10^{-3}	1.38 × 10^{-1}
	13*	0.99200	7.57 × 10^{-4}	9.86 × 10^{-5}	4.44 × 10^{-2}	0.98970	9.57 × 10^{-4}	1.12 × 10^{-4}	5.61 × 10^{-2}	0.96244	2.55 × 10^{-3}	2.14 × 10^{-4}	1.50 × 10^{-1}

(continued on next page)

Table 2 (continued)

Wells	t_d (days)	NARX-LM				NARX-BR				NARX-SCG			
		R ²	MAE	RMSE	RAE	R ²	MAE	RMSE	RAE	R ²	MAE	RMSE	RAE
25	0.99125	9.93 × 10^{-4}	1.73 × 10^{-4}	5.74 × 10^{-2}	0.99034	1.12 × 10^{-3}	3.12 × 10^{-4}	6.45 × 10^{-2}	0.94902	3.44 × 10^{-3}	4.67 × 10^{-4}	1.99 × 10^{-1}	
50	0.98679	1.53 × 10^{-3}	3.71 × 10^{-4}	8.45 × 10^{-2}	0.98525	1.44 × 10^{-3}	2.09 × 10^{-4}	8.21 × 10^{-2}	0.95043	3.42 × 10^{-3}	2.35 × 10^{-3}	1.94 × 10^{-1}	
100	0.98538	1.66 × 10^{-3}	1.43 × 10^{-4}	8.86 × 10^{-2}	0.97645	2.50 × 10^{-3}	9.70 × 10^{-4}	1.33 × 10^{-1}	0.90751	5.23 × 10^{-3}	1.35 × 10^{-4}	9.14 × 10^{-1}	

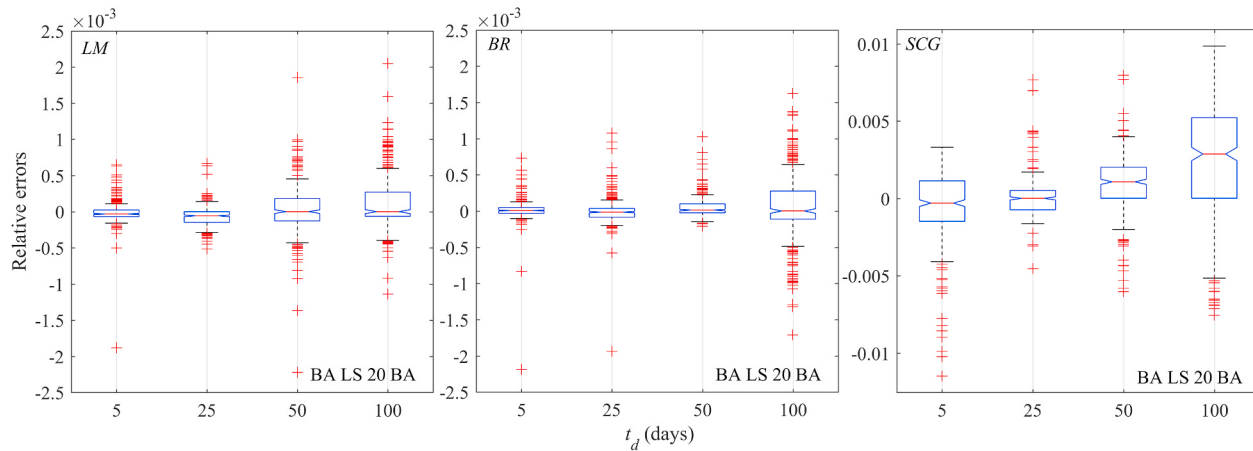


Fig. 7. GWL prediction for the well “BA LS 20 BA” - Model I: box plots of the relative errors. The lower end of each box plot denotes the 1st quartile (25th percentile), the upper end denotes the 3rd quartile (75th percentile). The “notch” represent the 95% confidence interval of the median. Whiskers extend from the box bottom to the smallest non-outlier and from the box top to the highest non-outlier.

evaluation metrics. As a supplement to what was described in the preliminary analysis, the statistical analysis was performed for the three training algorithms and for both Models I and II. The results showed that the inclusion of ET_p as a model input did not improve the accuracy of GWL prediction. Furthermore, lower performance of the NARX-SCG network was observed for 7 wells out of the 76 in total, with values of R^2 lower than 0.7, which is usually considered the minimum values for a proper prediction (Moore et al., 2018). For the NARX-BR network, the R^2 was higher than 0.9 for all the wells.

3.3. Sub-regional analysis

In order to better understand the differences from well to well in terms of GWL prediction performance, an extensive sub-regional analysis was performed, taking into account not only the well-described seasonal phenomena, such as precipitation and seasonal pumping, but also the four different hydrogeological structures in which the Apulia region is divided: Tavoliere, Gargano, Murgia, and Salento, with the last three that are karstic, making the Apulia region the host of the largest coastal karst Italian aquifers (Polemio, 2016).

Figs. 10, 12 and 14 on the left show the R^2 scattered maps for the different sub-regions. The location and features of the aquifers are reported in “Piano di Tutela delle Acque” (Apulia Region, 2019b). Figs. 10, 12 and 14 on the right show the RAE scattered maps for the different sub-regions, with a geological representation, similar to the one reported in Fig. 1 (ISPRA, 2011).

3.3.1. Gargano and Tavoliere

The Gargano area, as well as Murgia and Salento, is characterized by large carbonate aquifers, that are strongly influenced by karstic processes. These aquifers are hundreds of meters deep with a wide range of permeability (Cotecchia et al., 2005). In this area there are the following aquifers: Northern Gargano and Southern Gargano, affected by sea saltwater intrusion respectively from the northern and southern coast,

and the Central-Eastern Gargano. On the latter aquifer is placed the well “FG_3AIG” ($RMSE = 4.33 \times 10^{-6}$, $RAE = 1.83 \times 10^{-2}$) characterized by a remarkable average GWL equal to -200.11 m and a relatively low GWL fluctuation of 0.95 m. The latter is explained from the mountainous nature of the Gargano, with a very low level of anthropogenic activity in terms of the degree of groundwater utilization (Romanazzi et al., 2015). The time series (Fig. 11, upper chart) shows the limited but clearly visible effects, for this well, of seasonal phenomena, with a rise of the piezometric level during the winter months, characterized by higher rainfall and less water demand, and a lowering of the piezometric level during the summer, with less precipitation and higher water demand (GWL^* is the dimensionless groundwater level, normalized with respect to the minimum value, which corresponds to the lower water availability. A value of GWL^* equal to 1 indicates the deepest water level, therefore, to a reduction of GWL^* corresponds a rise of the piezometric level and vice-versa, see Equation (6)).

Partially overlapped with the Northern Gargano aquifer, there is a porous shallow aquifer, referred as Lesina Lake, whose waters are salinized due to the proximity to the coast (Cotecchia and Magri, 1966). On this aquifer is located the shallow well “FG_2 FP” ($RMSE = 4.74 \times 10^{-5}$, $RAE = 2.35 \times 10^{-1}$), with average GWL equal to -25.47 m, and fluctuation of the piezometric level equal to 0.72 m. The GWL time series (Fig. 11, middle chart) shows a singular trend, with a rise of the GWL during the years and a reduced impact of seasonal factors. This can mean a greater impact of the sea saltwater intrusion and of the aquifer recharge from the adjacent karst aquifer, with respect to the groundwater use for the seasonal pumping.

The Tavoliere area is mainly characterized by porous shallow aquifers, whose groundwater, that are limited by a clay bottom with thickness of hundreds of meters, flows in phreatic condition far from the sea (Northern-western Tavoliere) and is confined close to the Adriatic coast (Northern-eastern Tavoliere, Central-Southern Tavoliere and Southern-eastern Tavoliere). Unlike the Gargano aquifers, groundwater is not affected by salinization (Cotecchia, 2003). A well located in the

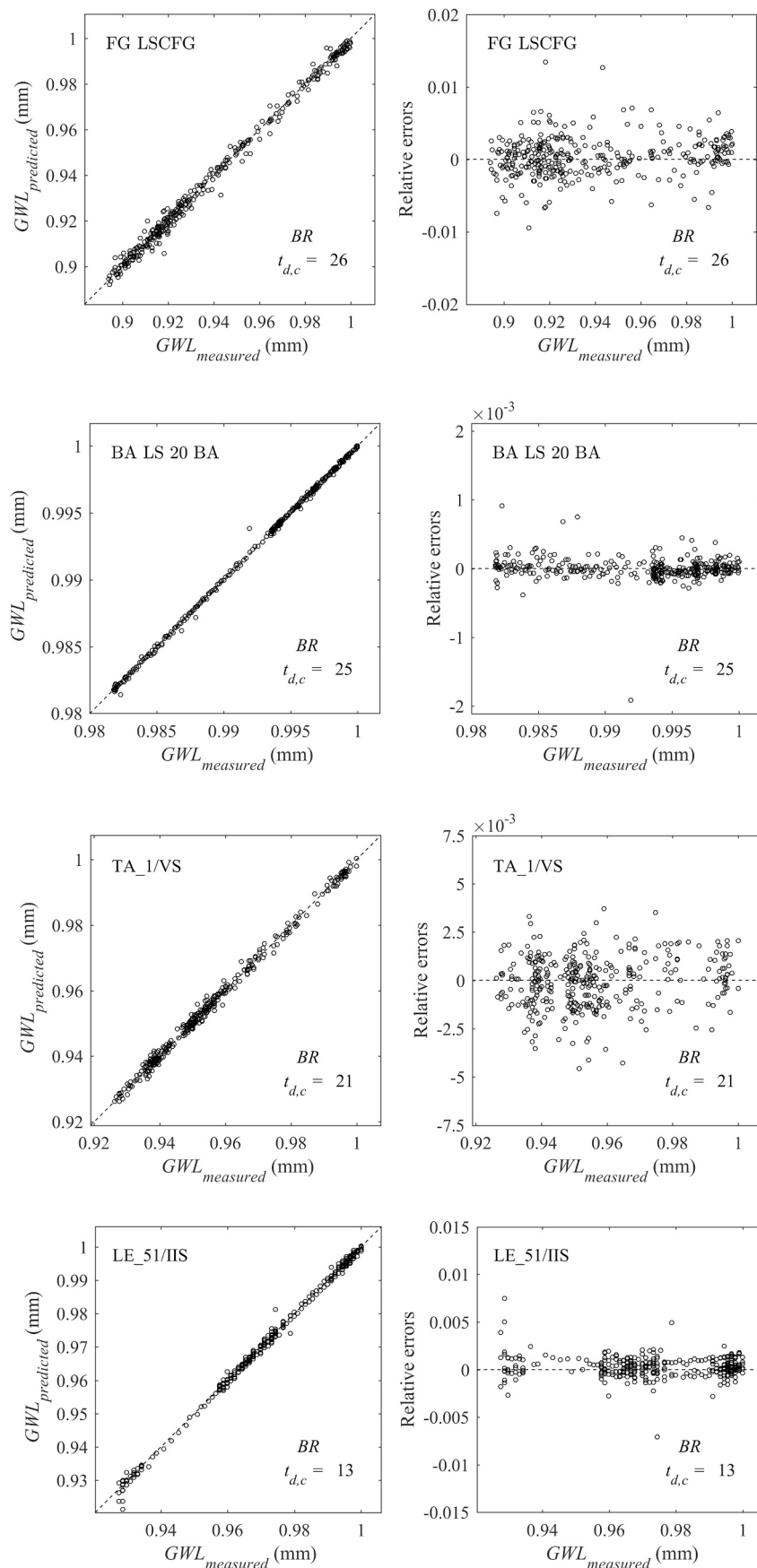


Fig. 8. GWL prediction (Model I, NARX-BR, computed time delay, validation step): in the left column, predicted versus measured values, in the right column, relative errors versus measured values.

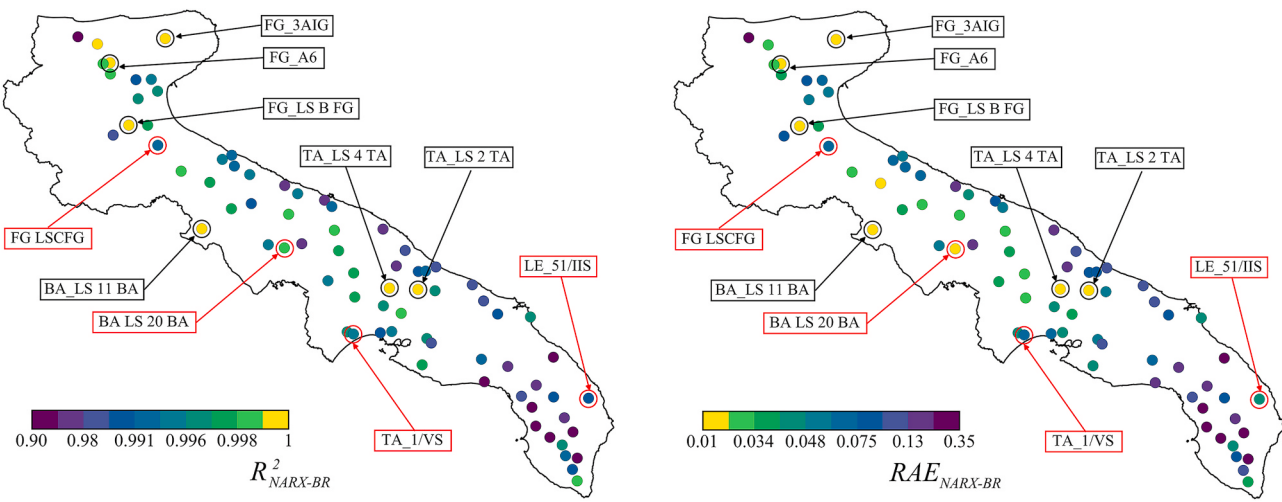


Fig. 9. Regional GWL prediction: R^2 scattered map (on the left); RAE scattered map (on the right).

Table 3

Regional prediction performance. NARX-BR, indicated in bold, provides the best prediction performance.

	NARX-LM				NARX-BR				NARX-SCG			
	R^2	MAE	RMSE	RAE	R^2	MAE	RMSE	RAE	R^2	MAE	RMSE	RAE
Model I												
Min.	0.89546	6.60 \times 10^{-5}	4.79 \times 10^{-6}	9.89 \times 10^{-3}	0.90774	6.25 \times 10^{-5}	4.33 \times 10^{-6}	1.08 \times 10^{-2}	0.27430	2.68 \times 10^{-4}	1.91 \times 10^{-5}	6.35 \times 10^{-2}
Max.	0.99988	4.16 \times 10^{-3}	2.98 \times 10^{-4}	3.46 \times 10^{-1}	0.99983	4.16 \times 10^{-3}	3.27 \times 10^{-4}	3.45 \times 10^{-1}	0.99363	1.51 \times 10^{-2}	1.06 \times 10^{-3}	9.32 \times 10^{-1}
Mean	0.98381	5.60 \times 10^{-4}	4.27 \times 10^{-5}	9.07 \times 10^{-2}	0.98561	5.19 \times 10^{-4}	4.13 \times 10^{-5}	8.64 \times 10^{-2}	0.87242	1.75 \times 10^{-3}	1.31 \times 10^{-4}	2.74 \times 10^{-1}
Std Dev	0.02319	7.30 \times 10^{-4}	5.49 \times 10^{-5}	7.58 \times 10^{-2}	0.02081	6.77 \times 10^{-4}	5.49 \times 10^{-5}	7.41 \times 10^{-2}	0.13406	2.33 \times 10^{-3}	1.69 \times 10^{-4}	1.64 \times 10^{-1}
Model II												
Min.	0.88311	5.96 \times 10^{-5}	3.03 \times 10^{-6}	1.75 \times 10^{-2}	0.90458	8.35 \times 10^{-5}	3.97 \times 10^{-8}	1.24 \times 10^{-2}	0.20005	3.24 \times 10^{-4}	2.39 \times 10^{-5}	7.68 \times 10^{-2}
Max.	0.99953	5.32 \times 10^{-3}	2.45 \times 10^{-3}	3.53 \times 10^{-1}	0.99966	4.66 \times 10^{-3}	2.17 \times 10^{-3}	3.25 \times 10^{-1}	0.99201	2.20 \times 10^{-2}	2.20 \times 10^{-2}	4.53 \times 10^{-1}
Mean	0.98028	7.07 \times 10^{-4}	2.00 \times 10^{-4}	1.01 \times 10^{-1}	0.98120	6.48 \times 10^{-4}	1.59 \times 10^{-4}	1.00 \times 10^{-1}	0.82819	2.68 \times 10^{-3}	1.22 \times 10^{-3}	4.62 \times 10^{-1}
Std Dev	0.02721	9.86 \times 10^{-4}	3.52 \times 10^{-4}	7.47 \times 10^{-2}	0.02407	8.89 \times 10^{-4}	3.15 \times 10^{-4}	7.88 \times 10^{-2}	0.17375	3.56 \times 10^{-3}	2.97 \times 10^{-3}	5.77 \times 10^{-1}

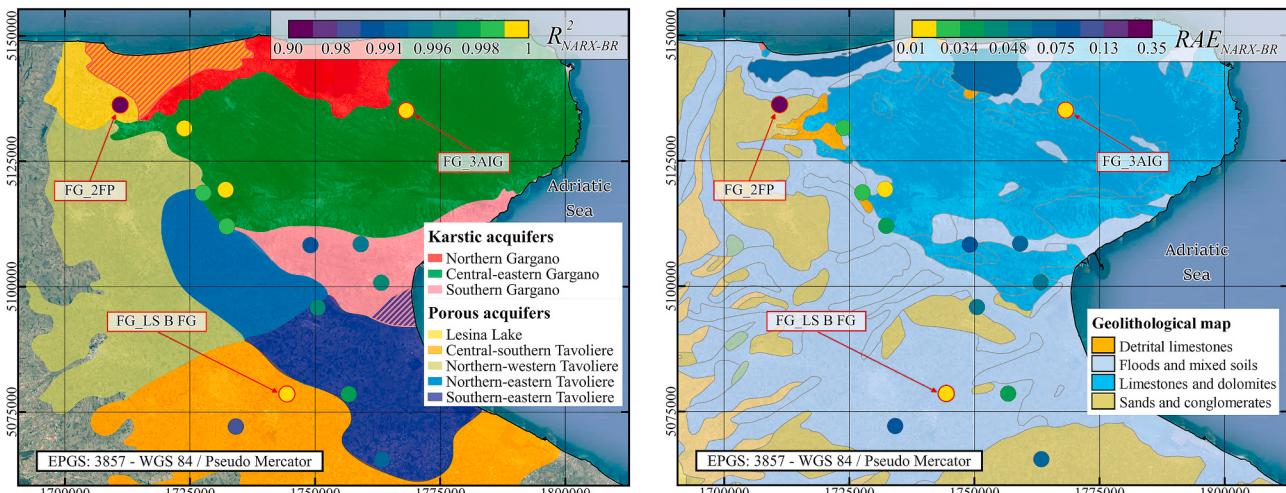


Fig. 10. GWL prediction in the Gargano and Tavoliere areas: R^2 scattered map with a representation of the aquifers (on the left); RAE scattered map with a geological representation (on the right).

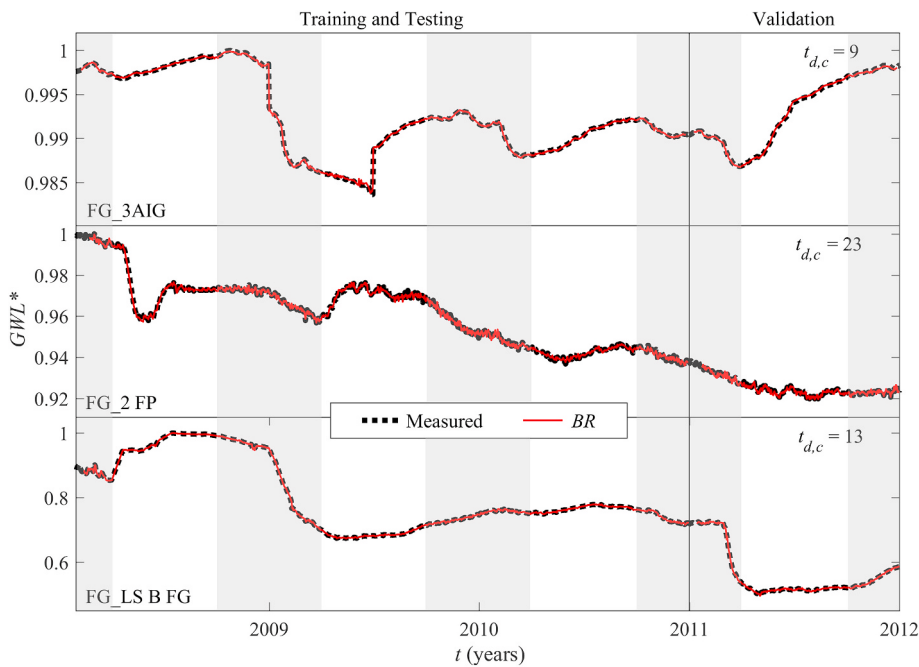


Fig. 11. GWL prediction for the wells “FG_3AIG”, “FG_2FP” and “FG_LS B FG”: comparison between measured and NARX-BR predicted values. The gray bands indicate the autumn-winter seasons while the white bands indicate the spring-summer seasons.

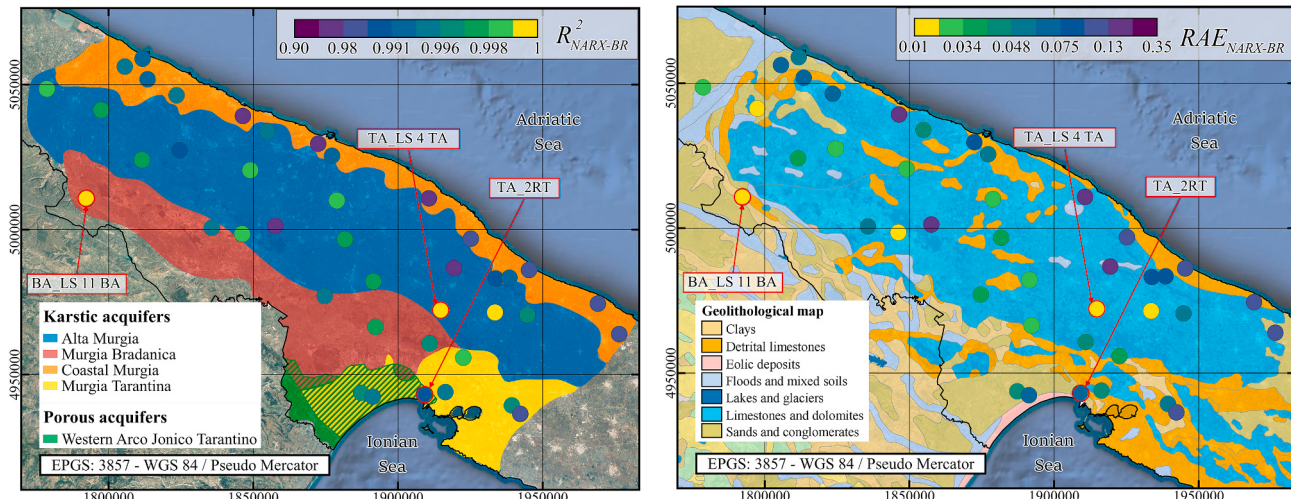


Fig. 12. Murgia GWL prediction: R^2 scattered map with a representation of the aquifers (on the left); RAE scattered map with a geolithological representation (on the right).

Central-Southern Tavoliere is “FG_LS B FG” ($RMSE = 9.02 \times 10^{-5}$, $RAE = 2.06 \times 10^{-2}$). It showed similar characteristics with the well “FG_2 FP” previously described, with a shallower level of the piezometric, equal to -10.49 m. Furthermore, a greater GWL fluctuation, equal to 1.76 m, was observed, in lines with several wells located on karst aquifers. Also for this well, a rising of the GWL was observed during the years. However, the lack of phenomena such as sea saltwater intrusion and recharge from karst aquifer, makes the impact of seasonal pumping clearly visible (Fig. 11, lower chart).

3.3.2. Murgia

The Murgia area corresponds to a karst plateau of rectangular shape, bordered by the Tavoliere plain to the north, the Adriatic Sea to the north-east, and by the Messapian threshold, that extends from Ionian Sea to Adriatic Sea, from the Salento peninsula to the south. The recharge of the Murgia karst aquifers occurs mainly from rainfall

infiltration (Cotecchia et al., 2005). Along the Adriatic side, based on the different degree of saline contamination, there are two different aquifers: Coastal Murgia, which is most affected by the sea saltwater intrusion being in direct contact with the Adriatic Sea, and Alta Murgia, that includes the internal portion of the karst aquifer between the Coastal Murgia and the hydrogeological watershed with the Murgia Bradanica aquifer. The latter is characterized exclusively by freshwater, not being in contact with sea water. On the aquifers of the Murgia Bradanica and Alta Murgia are located the deep wells “BA LS 11 BA” ($RMSE = 7.11 \times 10^{-6}$, $RAE = 1.45 \times 10^{-2}$), with average GWL equal to -260.41 m and GWL fluctuation of 2.99 m, and “TA LS 4 TA” ($RMSE = 8.91 \times 10^{-6}$, $RAE = 1.87 \times 10^{-2}$), with average GWL equal to -298.99 m and high GWL fluctuation of 6.75 m. Both wells are located in land used for growing grain and livestock farming, which involves a relevant water demand for the whole year. Nevertheless, the precipitation in the autumn and winter periods allow the aquifers to be recharged, which

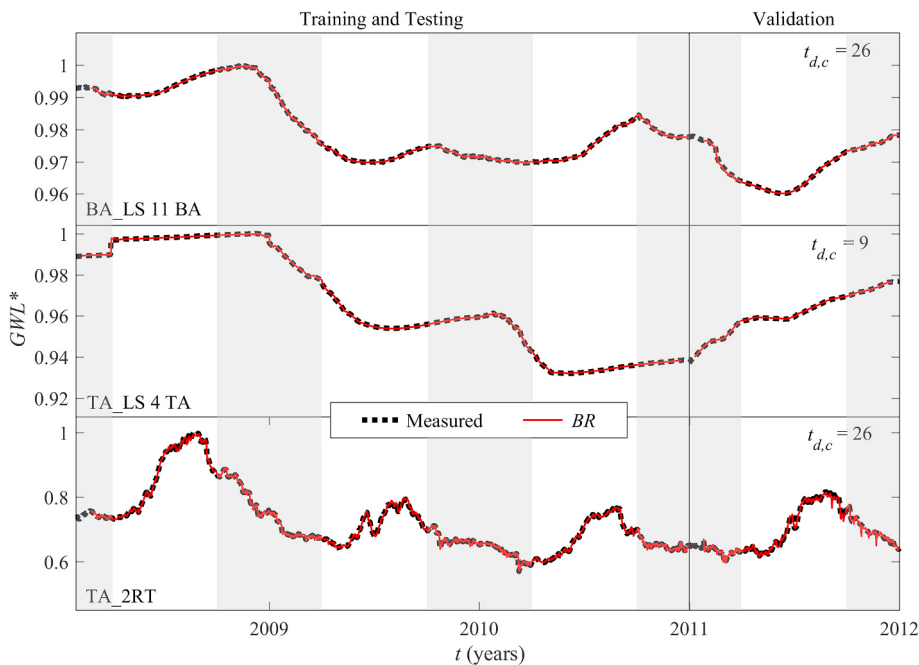


Fig. 13. GWL prediction for the wells “BA_LS 11 BA”, “TA_LS 4 TA” and “TA_2RT”: comparison between measured and NARX-BR predicted values. The gray bands indicate the autumn-winter seasons while the white bands indicate the spring-summer seasons.

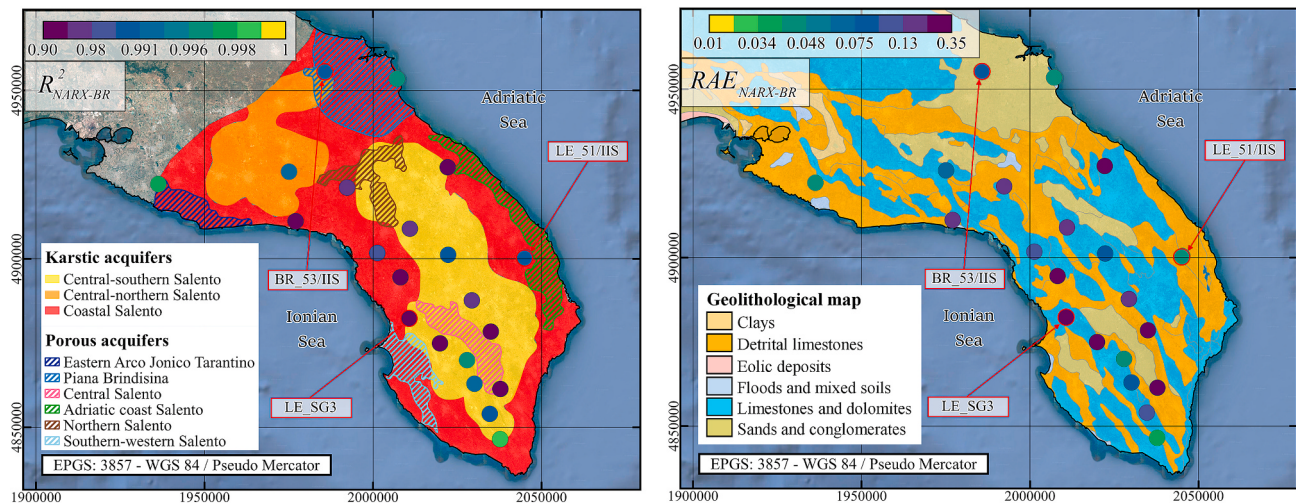


Fig. 14. Salento GWL prediction: R^2 scattered map with a representation of the aquifers (on the left); RAE scattered map with a geolithological representation (on the right).

involves a GWL^* reduction (Fig. 13, upper and middle charts), able to meet the water demand (GWL^* increase). Furthermore, the piezometric rise and lowering are relatively undisturbed, showing changes of sign in the piezometric fluctuation with frequencies that reach weeks for “BA_LS 11 BA” and several months for “TA_LS 4 TA” (Fig. 13, upper and middle charts).

Along the Ionian coast there is a multi-layered aquifer, which consist of the karst aquifer of Murgia Tarantina, whose waters are contaminated by sea saltwater intrusion, and a porous shallow aquifer, referred as Western Arco Jonico Tarantino. The distribution of the shallow aquifer that coincides mostly with that of terraced marine deposits, consisting in sands, conglomerates and eolian deposits (Maggiore, 1991, Fig. 12 on the right). On the latter aquifer is located the shallow well “TA_2RT” ($RMSE = 3.27 \times 10^{-4}$, $RAE = 7.39 \times 10^{-2}$), with average GWL equal to -3.18 m and low GWL fluctuation, equal to 0.41 m. The well, located in the countryside of Palagiano near the Tara spring, is affected both by the

inflows of freshwater from the nearby spring and from the seasonal phenomena (ISPRA, 2017). This emerges in the GWL^* time series, which shows fluctuation of the piezometric level with continuous changes of sign, with weekly or even daily frequencies (Fig. 13, lower chart).

3.3.3. Salento

Salento is a mainly flat area, bounded by the Adriatic and Ionian seas. It is characterized by extensive karst aquifers, representing a very important water resource for the area, which “float” for all their extensions on the sea saltwater, as there is an underground hydraulic connection between the Adriatic and Ionian seas (Cotecchia, 1958). The Salento groundwater balance is governed by two important features: the filtration inflow from the Murgia karst aquifers through the northern aquifer boundary and the outflow toward the sea (Giudici et al., 2012).

Along the entire coast line of Salento there is a karst aquifer, referred as “Coastal Salento”, whose waters are contaminated by sea saltwater

intrusion (Cotecchia et al., 2005, Fig. 14 on the left). On this aquifer the well "LE_51/IIS" ($RMSE = 1.03 \times 10^{-4}$, $RAE = 4.85 \times 10^{-2}$) is located. In comparison with the previously described Murgia and Gargano wells located in karst aquifer, the well "LE_51/IIS" showed a shallower piezometric level, equal to 8.98 m, and lower fluctuation, equal to 0.43 m, highlighting the singular features of the Salento karst aquifers (Fig. 15, upper charts).

A second karst aquifer in this area is the Central-Northern Salento, located close to the Messapian threshold, which receives significant freshwater contributions from the adjacent Murgia aquifer. This aquifer is superimposed in its western part by a porous shallow aquifer, referred to as Piana Brindisina, with the latter that also is extended above the karst aquifer Coastal Salento. The well "BR_53/IIS" ($RMSE = 1.45 \times 10^{-5}$, $RAE = 7.89 \times 10^{-2}$) is located in this shallow aquifer. Its average *GWL* was equal to 47.59 m, highlighting a greater depth of the piezometric level in the northern coastal area of Salento with respect to the central and southern ones (Fig. 15, middle chart). At the same time, a *GWL* fluctuation equal to 0.28 m was measured, the lowest in comparison with the previously described wells, showing continuous changes of the sign, with weekly frequency, in the raising or lowering of the piezometric level.

A third karst aquifer, indicated as Central-Southern Salento, is represented by the large area of freshwater located in the center of the Salento peninsula. This aquifer has indefinite and variables limits, with the latter that can approach or move away from the coast according to the hydrogeological balance between fresh groundwater and sea salt water. Therefore, to analyze the *GWL* fluctuations in this area, the well "LE_SG 3" ($RMSE = 1.29 \times 10^{-5}$, $RAE = 2.2 \times 10^{-1}$), located in proximity of the southern Coastal Salento area, was chosen. This well was characterized by a deeper average *GWL*, equal to 89.70 m, and the same *GWL* fluctuation, equal to 0.28 m, in comparison with "BR_53/IIS". These findings confirm the different characteristics of the karst aquifers of Salento, in particular in the central and southern areas, which are, in comparison with the karst aquifers of the Murgia and Gargano areas, shallower and probably affected by a greater impact of the sea saltwater intrusion on the piezometric level fluctuation. However, the latter aspect needs further specific and more in-depth studies.

4. Conclusion

This study assessed the capability of the NARX network in the prediction of the daily groundwater level for 76 monitoring wells in the entire Apulian territory. Two models were developed, namely, Model I which has a single input parameter (P), and Model II which has two input parameters (P and ET_p), in addition, of course, to previously observed groundwater levels. Overall, very accurate groundwater level predictions were achieved regardless of whether or not evapotranspiration is considered as an input parameter, confirming the better forecasting ability of the NARX networks compared to other ANNs used to predict the groundwater level, that require more input parameters for accurate predictions.

The comparison among three different training algorithms clearly shows that the Bayesian Regularization (*BR*) algorithm leads to prediction models with better forecasting accuracy and less marked performance decay as the time delay increases. The robustness of the *NARX-BR* network was evaluated in the regional analysis, achieving satisfactory values of the evaluation metrics also in the validation step, which proved to be the most challenging situation for the groundwater level prediction, not including evapotranspiration in the input variables (Model I) and assuming time delays equal to those computed.

Therefore, the *NARX-BR* network has proven to be a reliable tool for investigating the level fluctuation for wells located on different hydrogeological structures. In particular, the sub-regional analysis highlighted the differences among the wells located on deep and karst aquifers and the ones located on shallow porous aquifers. Wells located on deep karst aquifers show relatively undisturbed piezometric rise and fall, with changes of the sign in the piezometric fluctuation with weekly or monthly frequencies. On the other hand, shallow wells are often characterized by daily changes of the sign in the piezometric fluctuation. In addition, depending on the proximity to the sea or to a karst aquifer, that respectively involves sea saltwater intrusion or groundwater recharge process, wells with particular *GWL* time series trends are observed, characterized by a low impact of seasonal phenomena. Similar features are also observed for *GWL* in the shallow wells located on the karst aquifers of the Salento area.

The very good results obtained for the Apulia region recommend the

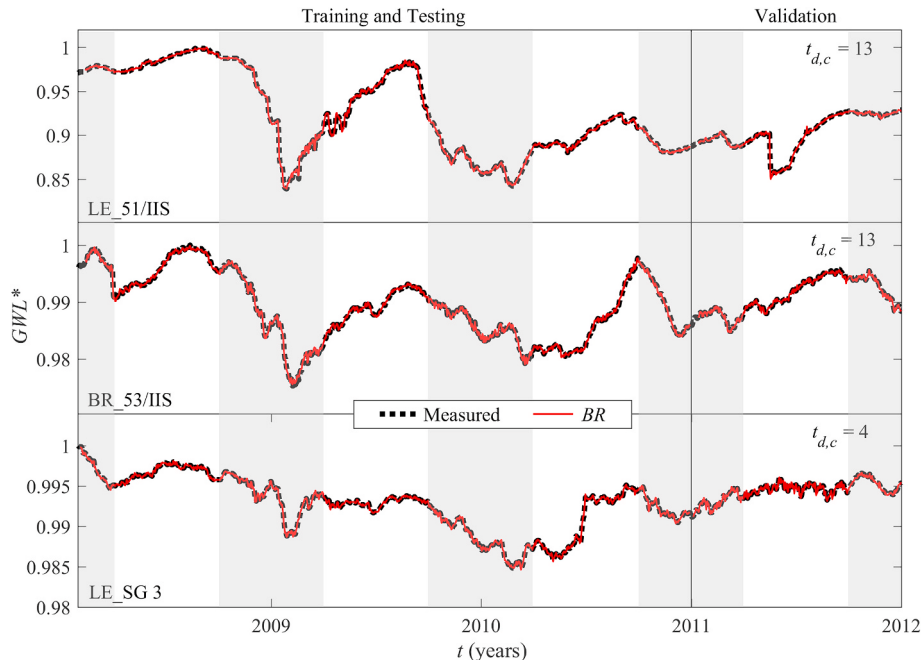


Fig. 15. *GWL* prediction for the wells "LE_51/IIS", "BR_53/IIS" and "LE_SG 3": comparison between measured and NARX-BR predicted values. The gray bands indicate the autumn-winter seasons while the white bands indicate the spring-summer seasons.

use of the NARX network for groundwater level prediction in other areas characterized by Mediterranean climate and karst phenomena, for which a proper management of water resources represents a socio-economic key factor for the next decades.

Credit author statement

Di Nunno Fabio – Methodology, Software, Formal analysis, Investigation, Writing - review & editing. Granata Francesco – Conceptualization, Validation, Supervision, Investigation, Writing - Review & Editing.

Declaration of competing interest

The authors declare that they have no known competing financial interests or personal relationships that could have appeared to influence the work reported in this paper.

References

- Adamowski, J., Chan, F.H., 2011. A wavelet neural network conjunction model for groundwater level forecasting. *J. Hydrol.* 407, 28–40. <https://doi.org/10.1016/j.jhydrol.2011.06.013>.
- Aksunaie, A.A., 2020. A nonlinear autoregressive modeling approach for forecasting groundwater level fluctuation in urban aquifers. *Water* 12 (3). <https://doi.org/10.3390/w12030820>.
- Apulia Region, 2019a. “Annali Idrologici - Parte I - 1921-2019. Civil Protection Section Apulia Region.
- Apulia Region, 2019b. “Piano di Tutela delle Acque – Aggiornamento 2015-2021. Water Protection Service.
- ASCE Task Committee on Application of Artificial Neural Networks in Hydrology, 2000. Artificial neural networks in hydrology. I: preliminary concepts. *J. Hydrol. Eng.* 5 (2), 115–123. [https://doi.org/10.1061/\(ASCE\)1084-0699\(2000\)5:2\(115\)](https://doi.org/10.1061/(ASCE)1084-0699(2000)5:2(115).
- Bishop, C.M., 1995. *Neural Networks for Pattern Recognition*. Oxford University Press.
- Chen, L.H., Chen, C.T., Pan, Y.G., 2010. Groundwater level prediction using SOM-RBFN multisite model. *J. Hydrol. Eng.* 15 (8), 624–631. [https://doi.org/10.1061/\(ASCE\)HE.1943-5584.0000218](https://doi.org/10.1061/(ASCE)HE.1943-5584.0000218).
- Chen, L.H., Chen, C.T., Lin, D.W., 2011. Application of integrated back-propagation network and self-organizing map for groundwater level forecasting. *J. Water Resour. Plann. Manag.* 137 (4), 352–365. [https://doi.org/10.1061/\(ASCE\)WR.1943-5452.0000121](https://doi.org/10.1061/(ASCE)WR.1943-5452.0000121).
- Chitsazan, M., Rahmani, G., Neyamadpour, A., 2015. Forecasting groundwater level by artificial neural networks as an alternative approach to groundwater modeling. *J. Geol. Soc. India* 85 (1), 98–106. <https://doi.org/10.1007/s12594-015-0197-4>.
- Cho, K.H., Sthiannopkao, S., Pachepsky, Y.A., Kim, K.W., Kim, J.H., 2011. Prediction of contamination potential of groundwater arsenic in Cambodia, Laos, and Thailand using artificial neural network. *Water Res.* 45 (17), 5535–5544. <https://doi.org/10.1016/j.watres.2011.08.010>.
- Cnr-Irsa, 2009. Progetto Tiziano - progetto del sistema di monitoraggio qualitativo e quantitativo dei corpi idrici sotterranei della Regione Puglia - relazione Finale sull'attività.
- Cotecchia, V., 1958. Sviluppi della teoria di Ghyben ed Herzberg nello studio idrogeologico della alimentazione e dell'impiego delle falde acqueifere, con riferimento a quella profonda delle Murge e del Salento. *Geotecnica* 6.
- Cotecchia, V., Magri, G., 1966. Idrogeologia del Gargano. *Geol. Appl. Idrogeol.* 1, 1–80.
- Cotecchia, V., 2003. Ricerca scientifica finalizzata all'analisi ed alla verifica dello stato quantitativo e qualitativo delle risorse idriche sotterranee nelle aree del Tavoliere di Foggia, del promontorio del Gargano e dell'Alta Murgia, al fine del possibile impiego nell'approvvigionamento idrico potabile della Regione Puglia. *Ministero delle Infrastrutture e dei Trasporti - Provveditorato alle Opere Pubbliche per la Puglia*.
- Cotecchia, V., Grassi, D., Polemio, M., 2005. Carbonate aquifers in Apulia and seawater intrusion. *G. Geol. Appl.* 1, 219–231. <https://doi.org/10.1474/GGA.2005-01.0-22.0022>.
- Cui, Y., Liao, Z., Wei, Y., Xu, X., Song, Y., Liu, H., 2020. The response of groundwater level to climate change and human activities in baotou city, China. *Water* 12. <https://doi.org/10.3390/w12041078>.
- Coulibaly, P., Anctil, F., Aravena, R., Bobee, B., 2001. Artificial neural network modeling of water table depth fluctuations. *Water Resour. Res.* 37 (4), 885–896. <https://doi.org/10.1029/2000WR900368>.
- Daliakopoulos, I.N., Coulibaly, P., Tsanis, I.K., 2005. Groundwater level forecasting using artificial neural networks. *J. Hydrol.* 309, 229–240. <https://doi.org/10.1016/j.jhydrol.2004.12.001>.
- De Filippis, G., Giudici, M., Margiotta, S., Mazzone, F., Negri, S., Vassena, C., 2013. Numerical Modeling of the Groundwater Flow in the Fractured and Karst Aquifer of the Salento Peninsula (Southern Italy). *AS/IT JGW*. <https://doi.org/10.7343/AS-016-013-0040>.
- De Filippis, G., Foglia, L., Giudici, M., Mehl, S., Margiotta, S., Negri, S.L., 2016. Seawater intrusion in karstic, coastal aquifers: current challenges and future scenarios in the Taranto area (southern Italy). *Sci. Total Environ.* 573, 1340–1351. <https://doi.org/10.1016/j.scitotenv.2016.07.005>.
- De Filippis, G., Margiotta, S., Caruso, F., Negri, S.L., 2020. Open questions about the hydrodynamic behaviour of the deep, coastal aquifer of the Salento peninsula (south-eastern Italy): coupling expert knowledge, data, and numerical modelling for testing hydrogeological conceptual models. *Sci. Total Environ.* 715. <https://doi.org/10.1016/j.scitotenv.2020.136962>.
- De Giglio, O., Napoli, C., Apollonio, F., Brigida, S., Marzella, A., Diella, G., Calia, C., Scrascia, M., Pacifico, C., Pazzani, C., Uricchio, V.F., Montagna, M.T., 2019. Occurrence of Legionella in groundwater used for sprinkler irrigation in Southern Italy. *Environ. Res.* 170, 215–221. <https://doi.org/10.1016/j.enres.2018.12.041>.
- Dixon, B., 2009. A case study using support vector machines, neural networks and logistic regression in a GIS to identify wells contaminated with nitrate-N. *Hydrogeol. J.* 17 (6), 1507–1520. <https://doi.org/10.1007/s10040-009-0451-1>.
- Dong, Y., Jiang, C., Suri, M.R., Pee, D., Meng, L., Rosenberg Goldstein, R.E., 2019. “Groundwater level changes with a focus on agricultural areas in the Mid-Atlantic region of the United States, 2002–2016. *Environ. Res.* 171, 193–203. <https://doi.org/10.1016/j.enres.2019.01.004>.
- Du, Y.C., Stephanus, A., 2018. Levenberg-marquardt neural network algorithm for degree of arteriovenous fistula stenosis classification using a dual optical photoplethysmography sensor. *Sensors* 18. <https://doi.org/10.3390/s18072322>.
- FAO, 1998. *Crop Evapotranspiration - Guidelines for Computing Crop Water Requirements*. FAO Irrigation and Drainage, p. 56.
- Fiorentino, G., Caldara, M., De Santis, V., D'Oronzo, C., Muntoni, I., Simone, O., Primavera, M., Radina, F., 2013. “Climate changes and human–environment interactions in the Apulia region of southeastern Italy during the Neolithic period. *Holocene* 23 (9), 1297–1316. <https://doi.org/10.1177/0959683613486942>.
- Foresee, F.D., Hagan, M.T., 1997. Gauss-Newton approximation to Bayesian learning, 3, 1930–1935. <https://doi.org/10.1109/ICNN.1997.614194>. Proceedings of International Conference on Neural Networks (ICNN '97).
- Giudici, M., Margiotta, S., Mazzone, F., Negri, S., Vassena, C., 2012. Modelling hydrostratigraphy and groundwater flow of a fractured and karst aquifer in a Mediterranean basin (Salento peninsula, southeastern Italy). *Environ. Earth Sci.* 67. <https://doi.org/10.1007/s12665-012-1631-1>.
- Granata, F., 2019. “Evapotranspiration evaluation models based on machine learning algorithms—a comparative study. *Agric. Water Manag.* 217, 303–315. <https://doi.org/10.1016/j.agwat.2019.03.015>.
- Granata, F., Gargano, R., de Marinis, G., 2020. Artificial intelligence based approaches to evaluate actual evapotranspiration in wetlands. *Sci. Total Environ.* 703. <https://doi.org/10.1016/j.scitotenv.2019.135653>.
- Guzman, S.M., Paz, J.O., Tagert, M.L.M., 2017. The use of NARX neural networks to forecast daily groundwater levels. *Water Resour. Manag.* 31, 1591–1603. <https://doi.org/10.1007/s11269-017-1598-5>.
- Guzman, S.M., Paz, J.O., Tagert, M.L.M., Mercer, A.E., 2018. Evaluation of seasonally classified inputs for the prediction of daily groundwater levels: NARX networks vs support vector machines. *Environ. Model. Assess.* 24, 223–234. <https://doi.org/10.1007/s10666-018-9639-x>.
- Hargreaves, G., Samani, Z., 1985. Reference crop evapotranspiration from temperature. *Appl. Eng. Agric.* 1 (2), 96–99. <https://doi.org/10.13031/2013.26773>.
- Hocking, M., Kelly, B.F.J., 2016. Groundwater recharge and time lag measurement through Versotols using impulse response functions. *J. Hydrol.* 535, 22–35. <https://doi.org/10.1016/j.jhydrol.2016.01.042>.
- Iannello, J.P., 1982. Time delay estimation via cross-correlation in the presence of large estimation errors. *IEEE Trans. Signal Process.* 30 (6), 998–1003. <https://doi.org/10.1109/tassp.1982.1163992>.
- ISPRA, 2011. *Carta Geologica d'Italia. Risoluzione 1:500.000*. Italian Institute for Environmental Protection and Research - Geological Survey of Italy.
- ISPRA, 2017. “Area Idrogeologica Dell’arco Ionico Tarantino, vol. 92. Memorie descrittive della Carta Geologica d’Italia.
- Juan, C., Genxu, W., Tianxu, M., 2015. Simulation and prediction of suprapermafrost groundwater level variation in response to climate change using a neural network model. *J. Hydrol.* 529, 1211–1220. <https://doi.org/10.1016/j.jhydrol.2015.09.038>.
- Khaki, M., Yusoff, I., Islami, N., 2015. Application of the artificial neural network and neuro-fuzzy system for assessment of groundwater quality. *Clean* 43, 551–560. <https://doi.org/10.1002/clen.201400267>.
- Lee, C.C., Sheridan, S.C., 2018. A new approach to modeling temperature-related mortality: non-linear autoregressive models with exogenous input. *Environ. Res.* 164, 53–64. <https://doi.org/10.1016/j.enres.2018.02.020>.
- Levenberg, K., 1944. A method for the solution of certain non-linear problems in least squares. *Q. Appl. Math.* 2 (2), 164–168. <https://doi.org/10.1090/qam/10666>.
- MacKay, D.J.C., 1992. Bayesian interpolation. *Neural Comput.* 4, 415–447. <https://doi.org/10.1162/neco.1992.4.3.415>.
- Maggiore, M., 1991. Aspetti idrogeologici degli acquiferi pugliesi in relazione alla ricarica artificiale. *Quad. IRSA* 94, 6.1–6.32.
- Marini, G., Fontana, N., Mishra, A., 2018. “Investigating drought in Apulia region, Italy using SPI and RDI.” *Theor. Appl. Climatol.* 1–15. <https://doi.org/10.1007/s00704-018-2604-4>.
- MathWorks, 2020. *MATLAB Deep Learning Toolbox Release 2020a*. Natick, Massachusetts, United States.
- Möller, M.F., 1993. A scaled conjugate gradient algorithm for fast supervised learning. *Neural Network*. 6 (4), 525–533. [https://doi.org/10.1016/S0893-6080\(05\)80056-5](https://doi.org/10.1016/S0893-6080(05)80056-5).
- Moore, D.S., Notz, W.I., Fligner, M.A., 2018. *The Basic Practice of Statistics*, eighth ed. W.H. Freeman and Company, p. 654.
- Parise, M., 2003. Flood history in the karst environment of Castellana-Grotte (Apulia, southern Italy). *Nat. Hazard Earth Sys* 3 (6), 593–604. <https://doi.org/10.5194/nhess-3-593-2003>.
- Polemio, M., 2005. Seawater intrusion and groundwater quality in the Southern Italy region of Apulia: a multi-methodological approach to the protection. In: *Progress in*

- Surface and Subsurface Water Studies at the Plot and Small Basin Scale, vol. 77, pp. 171–178.
- Polemio, M., Casarano, D., Limoni, P.P., 2009. "Karstic aquifer vulnerability assessment methods and results at a test site (Apulia, Southern Italy)", *Nat. Hazards Earth Syst. Sci.* 9 (4), 1461–1470. <https://doi.org/10.5194/nhess-9-1461-2009>.
- Polemio, M., 2016. Monitoring and management of karstic coastal groundwater in a changing environment (southern Italy): a review of a regional experience. *Water* 8 (4), 148. <https://doi.org/10.3390/w8040148>.
- Rajaee, T., Ebrahimi, H., Nourani, V., 2019. A review of the artificial intelligence methods in groundwater level modeling. *J. Hydrol.* 572, 336–351. <https://doi.org/10.1016/j.jhydrol.2018.12.037>.
- Romanazzi, A., Gentile, F., Polemio, M., 2015. Modelling and management of a Mediterranean karstic coastal aquifer under the effects of seawater intrusion and climate change. *Environ. Earth Sci.* 74, 115–128.
- Sahoo, G.B., Ray, C., Wade, H.F., 2005. Pesticide prediction in ground water in North Carolina domestic wells using artificial neural networks. *Ecol. Model.* 183 (1), 29–46. <https://doi.org/10.1016/j.ecolmodel.2004.07.021>.
- Sharma, B., Venugopalan, K., 2014. Comparison of neural network training functions for hematoma classification in brain CT images. *IOSR J. Comput. Eng.* 16 (1), 31–35. <https://doi.org/10.9790/0661-16123135>.
- Shiri, J., Kisi, O., Yoon, H., Lee, K.K., Nazemi, A.H., 2013. "Predicting groundwater level fluctuations with meteorological effect implications—a comparative study among soft computing techniques. *Comput. Geosci.* - UK 56, 32–44. <https://doi.org/10.1016/j.cageo.2013.01.007>.
- Tennyson, L., Settergren, C., Hansen, W., 1975. Sewage Effluent Irrigation Rates and Groundwater response." Symposium on Watershed Management by. ASCE Irrigation and Drainage Division, Logan, Utah, USA.
- Tulipano, L., Fidelibus, D.M., Panagopoulos, A., 2005. *Groundwater Management of Coastal Karstic Aquifers. COST*, p. 621.
- Wu, W., Dandy, G.C., Maier, H.R., 2014. Protocol for developing ANN models and its application to the assessment of the quality of the ANN model development process in drinking water quality modelling. *Environ. Model. Software* 54, 108–127. <https://doi.org/10.1016/j.envsoft.2013.12.016>.
- Wunsch, A., Liesch, T., Broda, S., 2018. Forecasting groundwater levels using nonlinear autoregressive networks with exogenous input (NARX). *J. Hydrol.* 567, 743–758. <https://doi.org/10.1016/j.jhydrol.2018.01.045>.
- Yu, H., Wilamowski, B.M., 2011. *Levenberg-Marquardt Training - Industrial Electronics Handbook*. CRC Press, 12-21-12-15.
- Zhang, J., Zhang, X., Niu, J., Hu, B.X., Soltanian, M.R., Qiu, H., Yang, L., 2019. Prediction of groundwater level in seashore reclaimed land using wavelet and artificial neural network-based hybrid model. *J. Hydrol.* 577 <https://doi.org/10.1016/j.jhydrol.2019.123948>.